Unsteady turbulent line plumes

Andrew J. Hogg[1,†], **Edward J. Goldsmith**[2] **and Mark J. Woodhouse**[1,3]

[1]School of Mathematics, University of Bristol, University Walk, Bristol BS8 1TW, UK

[2]Department of Mathematics, University College London, Gower Street, London WC1E 6BT, UK

[3]School of Earth Science, University of Bristol, Wills Memorial Building, Queens Road,
Bristol BS8 1RJ, UK

The unsteady ascent of a buoyant, turbulent line plume through a quiescent, uniform environment is modelled in terms of the width-averaged vertical velocity and density deficit. It is demonstrated that for a well-posed, linearly stable model, account must be made for the horizontal variation of the velocity and the density deficit; in particular the variance of the velocity field and the covariance of the density deficit and velocity fields, represented through shape factors, must exceed threshold values, and that models based upon 'top-hat' distributions in which the dependent fields are piecewise constant are ill-posed. Numerical solutions of the nonlinear governing equations are computed to reveal that the transient response of the system to an instantaneous change in buoyancy flux at the source may be captured through new similarity solutions, the form of which depend upon both the ratio of the old to new buoyancy fluxes and the shape factors.

1. Introduction

Line plumes arise when buoyant fluid emerges from an extended line source. Their two-dimensional ascent though the environment is driven by the gravitational force associated with their density deficit and is strongly affected by the mixing that occurs with the surrounding environmental fluid. Their dynamics share many features with axisymmetric plumes, which emerge from point sources (Morton, Taylor & Turner 1956; Turner 1973). However, the planar geometry affects the evolution of bulk properties in different ways to their axisymmetric counterparts, and leads to different dependences on the source conditions (Rouse, Yih & Humphreys 1952; van den Bremer & Hunt 2014; Craske 2017). Line plumes are of direct interest in geophysical and industrial settings: examples include the emission of hot material from volcanic fissures on land (Stothers 1989) and at mid-ocean ridges (Woods 2010); the mechanics of fire plumes from line sources (Lee & Emmons 1961); polar leads of saline water along planar cracks in ice sheets (Ching, Fernando & Robles 1995); and ventilation flows within buildings (van den Bremer & Hunt 2014).

† Email address for correspondence: a.j.hogg@bristol.ac.uk

In this paper we develop a time-dependent model of line plumes, based upon an integral model of the rise velocity and density deficit relative to the environment, averaged over the width of the plume. Compared to their axisymmetric counterparts, line plumes and their time-dependent motion have received relatively little study (van den Bremer & Hunt 2014), although Craske (2017) has recently analysed the time-dependent dynamics of line jets. In the current study we show that a model which assumes 'top-hat' profiles of velocity and density, in which both fields are assumed to be constant within a defined width, is ill-posed; this result is analogous to axisymmetric plumes (Scase & Hewitt 2012). Instead, one must account for the distributions of velocity and density, which in this width-averaged formulation are represented through shape factors that are related to the variance of the velocity field and the covariance between the density and velocity fields. The inclusion of these factors plays a crucial role in the behaviour of the model (Craske & van Reeuwijk 2016; Woodhouse, Phillips & Hogg 2016). We show that there are certain values of these two shape factors that lead to ill-posedness and other values which lead to regimes within which the time-dependent model supports stable steady solutions that are not susceptible to disturbances that grow in the far field. If indeed only the distribution of the velocity field is included (and the density distribution assumed to be 'top-hat'-like) then the model is only stable if the variance exceeds a critical value that we determine. This is the analogous result for line plumes that was found for axisymmetric plumes (Woodhouse *et al.* 2016), although the critical value differs in this different geometry. In this study, however, we extend the analysis to characterise more completely the significance of including distributions in both the velocity and density fields.

We also examine the nonlinear, unsteady adjustment associated with an instantaneous change in the buoyancy flux per unit width at the source. Such a change leads to a transient pulse that propagates through the domain as the system adjusts from one steady state to another. The transition is captured numerically by integrating the governing system of partial differential equations (in a regime for which they are well-posed and stable). However, the transition is more insightfully found quasi-analytically in terms of a similarity solution. The similarity solution arises because for an instantaneous change in buoyancy flux per unit width, there is no external length scale imposed upon the system. Its form depends upon the ratio of the old to the new buoyancy fluxes at the source, as well as the values of the shape factors. The solution may feature shocks, over which the variables change discontinuously, and critical points at which the gradients change discontinuously. We show how to construct these new similarity solutions and describe how the phenomena that they exhibit may be classified in terms of the ratio of the old to new buoyancy fluxes and the shape factors. The solutions are distinct from their axisymmetric counterparts in that the gearing between spatial and temporal variables is different (Woodhouse *et al.* 2016). Moreover they differ strongly from the 'separable' similarity solutions reported by Scase *et al.* (2006) and Craske & van Reeuwijk (2016), and more recently for line jets by Craske (2017) in that they satisfy all the boundary conditions for the motion generated by an instantaneous change in the buoyancy flux per unit width.

The paper is structured as follows. First we formulate the width-averaged governing equations and identify steady states (§ 2). We then demonstrate ill-posedness and linear instability if the shape factors adopt certain values, behaviour which is confirmed through numerical integration of the nonlinear governing equations (§ 3). Notably in this section we show that the assumption of 'top-hat' profiles leads to an

ill-posed system of equations. Then in the regimes where the governing equations are well-posed and linearly stable, we compute the response to an instantaneous change in buoyancy flux per unit width at the source and construct the underlying similarity solutions for this transition (§ 4). Brief conclusions are given in § 5. The paper also includes four appendices. In appendix A, we present a derivation of the governing equations and evaluate the shape factors if both the vertical velocity and reduced gravity (which encompasses the density deficit) adopt Gaussian distributions. We also show how different assumptions about the representation of the turbulent motions leads to a different integral model (Craske & van Reeuwijk 2016; Craske 2017), although shape factors will still be shown to play a vital role in this alternative formulation. In appendix B, we examine the linearised evolution, and find closed form solutions, arising from harmonic perturbations to the source of a line plume in the special case where the vertical velocity field adopts a top-hat distribution. In appendix C, we extend our linear stability analysis to an alternative model of line plumes, built on the study of line jets by Craske (2017). For this approach, we also demonstrate ill-posedness and regimes of linear stability that depend on the shape factors that occur within the alternative model. These results employ the mathematical framework developed in § 3 and reiterate the need to capture the distributions of velocity and reduced gravity within integral models of line plumes. Finally, in appendix D, we present the additional results from numerical integration of the nonlinear governing equations and the underlying similarity solutions in response to an instantaneous change in the buoyancy flux per unit width at the source. These results add to the phenomenology reported in § 4.

2. Governing equations

The two-dimensional, buoyancy-driven ascent of fluid through an environment of uniform density ρ_0 from a line source at $z = 0$, issuing fluid of density ρ_1 $(\rho_1 < \rho_0)$ is modelled in terms of the half-width of the mobile fluid, b, the vertical velocity, w, and the reduced gravity, $g' = (\rho_0 - \rho_p)g/\rho_0$, where ρ_p is the density of the plume and g is the magnitude of gravitational acceleration. The coordinate axes are aligned with x horizontal and z vertical (upwards), and the relative density of the plume fluid is sufficiently small $(\rho_0 - \rho_p)/\rho_0 \ll 1$) so that the motion is modelled under the Boussinesq approximation. On the assumption that the plume is relatively narrow so that the length scale of horizontal motion is much less than the length scale of vertical motion and consequentially, vertical pressure gradients are solely hydrostatic (Linden 2000), and that viscous processes are negligible, integral expressions that represent conservation of mass, balance of vertical momentum and evolution of reduced gravity are given by

$$\frac{\partial b}{\partial t} + \frac{\partial}{\partial z} \int_0^b w \, \mathrm{d}x = u_e, \tag{2.1}$$

$$\frac{\partial}{\partial t} \int_0^b w \, \mathrm{d}x + \frac{\partial}{\partial z} \int_0^b w^2 \, \mathrm{d}x = \int_0^b g' \, \mathrm{d}x, \tag{2.2}$$

$$\frac{\partial}{\partial t} \int_0^b g' \, \mathrm{d}x + \frac{\partial}{\partial z} \int_0^b g'w \, \mathrm{d}x = 0, \tag{2.3}$$

where u_e is the entrainment velocity, representing the rate at which environmental fluid is engulfed into the line plume per unit area. (Axisymmetric versions of these

106 *A. J. Hogg, E. J. Goldsmith and M. J. Woodhouse*

equations were developed by Scase & Hewitt (2012) and Woodhouse *et al.* (2016) and in appendix A, we derive these width-integrated expressions relevant for line plumes.) Crucially there is mixing between the environmental and buoyant fluids as the plume ascends due to the action of turbulent eddies and, following the seminal work of Morton *et al.* (1956), we invoke the entrainment assumption and write $u_e = \alpha w$, where α is a dimensionless constant. We comment that other studies have adopted different modelling strategies for representing the dynamics of turbulent plumes and in particular the mechanics of entrainment (Priestley & Ball 1955; Kaminski, Tait & Carazzo 2005; Craske & van Reeuwijk 2016). These studies have formulated expressions for the transport, production and loss of mean kinetic energy, averaged over the horizontal cross-section of the plume and have then made a closure for the turbulent terms to form an integral model (see, for example, Craske & van Reeuwijk 2016). An important outcome of these approaches is that the entrainment coefficient emerges as a consequence of the modelling; it is not constant but is a function of the dependent variables and their gradients. These alternatives could be substituted within the modelling framework that follows, and the model of Craske (2017) extended to line plumes, is analysed in appendix C. To derive the width-averaged form, we introduce

$$\int_0^b w \, dx = b\overline{w} \quad \text{and} \quad \int_0^b g' \, dx = b\overline{g'}. \qquad (2.4a,b)$$

These expressions define the width-averaged vertical velocity and reduced gravity. We must also model the fluxes of momentum and buoyancy

$$\int_0^b w^2 \, dx = Sb\overline{w}^2 \quad \text{and} \quad \int_0^b g'w \, dx = S_f b\overline{w}\,\overline{g'}, \qquad (2.5a,b)$$

where S and S_f are 'shape factors', which differ from unity when the dependent fields differ from 'top-hat' profiles (Craske & van Reeuwijk 2016; Woodhouse *et al.* 2016). In particular using (2.4), we note that

$$(S-1)b\overline{w}^2 = \int_0^b w^2 \, dx - b\overline{w}^2 = \int_0^b (w - \overline{w})^2 \, dx \geqslant 0, \qquad (2.6)$$

and so $S \geqslant 1$. Also we find that

$$(S_f - 1)b\overline{w}\,\overline{g'} = \int_0^b (g' - \overline{g'})(w - \overline{w}) \, dx, \qquad (2.7)$$

and therefore if the distributions of the reduced gravity and velocity fields are positively correlated then we anticipate $S_f \geqslant 1$ (Rouse *et al.* 1952; Anwar 1969); we focus on this regime in what follows (§§ 3 and 4), although we derive the results quite generally. (In appendix A we compute the shape factors on the assumption that the velocity and reduced gravity fields adopt Gaussian distributions about the centreline of the plume.) Provided the shape factors are constant, the governing system for b, $\overline{w}$ and $\overline{g'}$ is then given by

$$\frac{\partial b}{\partial t} + \frac{\partial}{\partial z}(b\overline{w}) = \alpha\overline{w}, \qquad (2.8)$$

$$\frac{\partial}{\partial t}(b\overline{w}) + S\frac{\partial}{\partial z}(b\overline{w}^2) = b\overline{g'}, \qquad (2.9)$$

$$\frac{\partial}{\partial t}(b\overline{g'}) + S_f\frac{\partial}{\partial z}(b\overline{w}\,\overline{g'}) = 0. \qquad (2.10)$$

https://doi.org/10.1017/jfm.2018.698 Published online by Cambridge University Press

This system is the natural generalisation to planar geometry of the time-dependent model for axisymmetric plumes (Woodhouse *et al.* 2016). These governing equations (2.8)–(2.10) form a strictly hyperbolic set of equations when $S > 1$ and $S_f \neq S \pm \sqrt{S^2 - S}$ with characteristic directions given by

$$\frac{dz}{dt} = S_f \overline{w} \quad \text{and} \quad \frac{dz}{dt} = (S \pm \sqrt{S^2 - S})\overline{w}. \tag{2.11a,b}$$

When $S = 1$ or $S_f = S \pm \sqrt{S^2 - S}$, the system is parabolic. These characteristic speeds are identical to the those for axisymmetric plumes up to a constant multiplicative factor (Woodhouse *et al.* 2016). When the system is hyperbolic, there may be solutions with discontinuities. Assuming the discontinuity is at $x = x_s(t)$, the jump conditions across shocks are given by

$$[b(\overline{w} - \dot{x}_s)]_{x_s^-}^{x_s^+} = 0, \quad [b\overline{w}(S\overline{w} - \dot{x}_s)]_{x_s^-}^{x_s^+} = 0 \quad \text{and} \quad [b\overline{g'}(S_f\overline{w} - \dot{x}_s)]_{x_s^-}^{x_s^+} = 0. \tag{2.12a--c}$$

These conditions conserve mass, momentum and buoyancy over the shock, respectively. In the special case $S_f = 1$ there are two types of shocks satisfying these conditions. In one type the vertical velocity, $\overline{w}$, and width of the line plume, b, are discontinuous, but the reduced gravity $\overline{g'}$ is continuous. In the other, termed a contact discontinuity, the vertical velocity equals the shock speed ($\overline{w} = \dot{x}_s$) and consequentially, the width must be continuous, but no condition is implied for the reduced gravity. As with the shallow water equations for fluid flows (e.g. Whitham 1974), we anticipate that terms neglected in the width-averaged plume equations (2.1)–(2.3), such as streamwise diffusion due to turbulent processes, will modify the structure of the solutions close to the discontinuities. However, away from these locations, and treated on length scales commensurate with the rest of the motion, the jump conditions (2.12) express conservation principles over the shock.

An important steady state of (2.8)–(2.10) corresponds to the motion generated by a sustained buoyancy flux at the line source. In this situation we enforce the 'pure plume' source conditions of a constant buoyancy flux per unit width, but vanishing mass and momentum fluxes at the origin ($S_f b \overline{w} \overline{g'} \to f_1$, $b\overline{w} \to 0$ and $b\overline{w}^2 \to 0$ as $z \to 0$, where $2f_1$ denotes the constant buoyancy flux at the source). This steady state was derived by Lee & Emmons (1961) for $S = S_f = 1$ and is only slightly modified by the inclusion of shape factors, S and S_f. It is given by

$$b = \alpha z, \quad \overline{w} = \left(\frac{f_1}{\alpha S S_f}\right)^{1/3} \quad \text{and} \quad \overline{g'} = \left(\frac{S f_1^2}{\alpha^2 S_f^2}\right)^{1/3} \frac{1}{z}. \tag{2.13a--c}$$

It is noteworthy that pure plume source conditions do not impose an independent length scale on the flow and consequently the dimensional dependences are determined solely in terms of the buoyancy flux per unit width, f_1, and the distance from the source, z (see Rouse *et al.* 1952). Thus the plume half-width grows linearly with distance from the source at a rate determined by the entrainment coefficient and is independent of the imposed buoyancy flux per unit width (see, for example, Morton *et al.* (1956), Turner (1973)). The velocity of the steady line plume remains constant at the value determined by the source condition. This is in contrast to axisymmetric plumes from a point source for which the velocity decreases with distance from the source as $z^{-1/3}$ (Morton *et al.* 1956) and to line jets (where there is no density difference but a non-zero momentum flux per unit width at the source) for which

the velocity decays as $z^{-1/2}$ (Bradbury 1965). This illustrates the delicate balance in steady line plumes with the buoyancy forces that accelerate the fluid being in balance with the momentum drag due to the entrainment and acceleration of ambient fluid. In what follows we examine the time-dependent behaviour when the source condition is altered from an established steady pure plume.

3. Unsteady evolution: well-posedness and linear stability

We analyse the unsteady behaviour of line plumes and to this end, it is convenient to introduce dimensionless independent variables and to redefine the dependent variables such that the steady state (2.13) is scaled out. We introduce $\tau = t/T$, where T is a relevant time scale of the motion, potentially set by time-dependent source conditions, and the dimensionless spatial variable is given by $\xi = z(\alpha SS_f/f_1)^{1/3}T^{-1}$. The following dimensionless dependent variables are introduced:

$$b = \alpha z \hat{b}(\xi, \tau), \quad b\overline{w} = \left(\frac{\alpha^2 f_1}{SS_f}\right)^{1/3} z\hat{q}(\xi, \tau) \quad \text{and} \quad b\overline{g'} = \left(\frac{\alpha Sf_1^2}{S_f^2}\right)^{1/3} \hat{g}(\xi, \tau). \quad (3.1a\text{-}c)$$

The governing equations can then be written in compact form by introducing $\boldsymbol{q} = (\hat{b}, \hat{q}, \hat{g})$ so that

$$\frac{\partial \boldsymbol{q}}{\partial \tau} + \begin{pmatrix} 0 & 1 & 0 \\ -S\hat{q}^2/\hat{b}^2 & 2S\hat{q}/\hat{b} & 0 \\ -S_f\hat{g}\hat{q}/\hat{b}^2 & S_f\hat{g}/\hat{b} & S_f\hat{q}/\hat{b} \end{pmatrix} \frac{\partial \boldsymbol{q}}{\partial \xi} = \frac{1}{\xi} \begin{pmatrix} \hat{q}(1-\hat{b})/\hat{b} \\ S(\hat{g} - \hat{q}^2/\hat{b}) \\ 0 \end{pmatrix}. \quad (3.2)$$

The steady state (2.13) corresponds to $\boldsymbol{q} = (1, 1, 1)$ and the buoyancy flux per unit width is $S_f b\overline{w}\overline{g'} = f_1\hat{j}$, where the dimensionless flux is denoted by $\hat{j} \equiv \hat{g}\hat{q}/\hat{b}$.

We now consider the linear stability of the steady state in response to the introduction of small perturbations in the source conditions. Thus we write $\boldsymbol{q} = (1, 1, 1) + \epsilon \boldsymbol{q}_1$, where ϵ is a small ordering parameter. We assume a harmonic perturbation at the source with angular frequency ω (so that $T = 1/\omega$) and the linearised solution can be written as $\boldsymbol{q}_1 = \exp(\phi(\xi) + i\tau)\boldsymbol{\psi}(\xi)$. To determine linear stability, we must find the behaviour of the dependent variables in the far field (Woodhouse *et al.* 2016). The linearised governing equations are given by

$$\boldsymbol{A}\frac{d\boldsymbol{\psi}}{d\xi} + \left(\boldsymbol{A}\frac{d\phi}{d\xi} + \boldsymbol{C}\frac{1}{\xi} + i\boldsymbol{I}\right)\boldsymbol{\psi} = 0, \quad (3.3)$$

where $\boldsymbol{I}$ is the identity matrix and the matrices $\boldsymbol{A}$ and $\boldsymbol{C}$ are given by

$$\boldsymbol{A} = \begin{pmatrix} 0 & 1 & 0 \\ -S & 2S & 0 \\ -S_f & S_f & S_f \end{pmatrix} \quad \text{and} \quad \boldsymbol{C} = \begin{pmatrix} 1 & 0 & 0 \\ -S & 2S & -S \\ 0 & 0 & 0 \end{pmatrix}. \quad (3.4a,b)$$

We seek expansions in the far field ($\xi \gg 1$) of the form

$$\phi = -i\lambda\xi + \sigma \log \xi + \frac{\gamma}{\xi} \ldots \quad \text{and} \quad \boldsymbol{\psi} = \boldsymbol{\psi}_0 + \frac{1}{\xi}\boldsymbol{\psi}_1 + \frac{1}{\xi^2}\boldsymbol{\psi}_2 \ldots \quad (3.5a,b)$$

We substitute (3.5) into (3.3) and equate successive powers of ξ^{-1}. At $O(1)$ we find that $\lambda = \lambda_i$, where $1/\lambda$ are eigenvalues of the matrix $\boldsymbol{A}$ and that $\boldsymbol{\psi}_0 = \boldsymbol{e}_{Ri}$ are the

associated eigenvectors. The eigenvalues, λ_i, and left and right eigenvectors, denoted $\boldsymbol{e}_{Li}$ and $\boldsymbol{e}_{Ri}$, respectively ($i = 1, 2, 3$), are given by

$$\lambda_1 = 1/S_f, \quad \boldsymbol{e}_{L1}^T = (S_f(S - S_f), S_f(S_f - 1), (S_f - S)^2 + S(1 - S)), \tag{3.6}$$

$$\boldsymbol{e}_{R1}^T = (0, 0, 1), \tag{3.7}$$

$$\lambda_{2,3} = 1 \pm \frac{\sqrt{S^2 - S}}{S}, \quad \boldsymbol{e}_{L2,3}^T = (-S\lambda_{2,3}, 1, 0), \tag{3.8}$$

$$\boldsymbol{e}_{R2,3}^T = (\lambda_{2,3}(S_f\lambda_{2,3} - 1), S_f\lambda_{2,3} - 1, S_f\lambda_{2,3}(\lambda_{2,3} - 1)). \tag{3.9}$$

We observe that

$$\boldsymbol{e}_{L1}^T \boldsymbol{A} \boldsymbol{e}_{R1} = S_f((S_f - S)^2 + S(1 - S)), \tag{3.10}$$

an expression that vanishes when $S_f = S \pm \sqrt{S^2 - S}$ (i.e. when two of the characteristics coincide). Also we find that

$$\boldsymbol{e}_{Li}^T \boldsymbol{A} \boldsymbol{e}_{Ri} = -2S(\lambda_i - 1)(S_f\lambda_i - 1) \quad \text{for } i = 2, 3. \tag{3.11}$$

This expression vanishes when $S = 1$. It will be shown below when $S = 1$ or when $S_f = S \pm \sqrt{S^2 - S}$ that the subsequent analysis fails and that these cases require special attention; in these situations the system of governing equations (3.2) is no longer hyperbolic.

At $O(1/\xi)$, we apply the solvability condition and this yields

$$\sigma_i \boldsymbol{e}_{Li} \boldsymbol{A} \boldsymbol{e}_{Ri} + \boldsymbol{e}_{Li} \boldsymbol{C} \boldsymbol{e}_{Ri} = 0, \tag{3.12}$$

for $i = 1, 2, 3$. Thus we deduce that provided $\boldsymbol{e}_{Li} \boldsymbol{A} \boldsymbol{e}_{Ri}$ is non-vanishing,

$$\sigma_1 = \frac{S(S_f - 1)}{(S - S_f)^2 + S(1 - S)} \tag{3.13}$$

$$\text{and} \quad \sigma_{2,3} = -2 + \frac{S(2S - 1) \pm (S_f - 2S)\sqrt{S^2 - S}}{2S(S \mp \sqrt{S^2 - S} - S_f)}. \tag{3.14}$$

We note straightaway that this perturbative solution has failed when $S_f = S \pm \sqrt{S^2 - S}$ since σ_1 and one of σ_2 and σ_3 are not defined at this value; this condition corresponds to the coincidence of two of the characteristic curves. However, when $S > 1$ and $S_f \neq S \pm \sqrt{S^2 - S}$, the solutions grow or decay in the far field in proportion to ξ^{σ_i}. These solutions due to a harmonic disturbance of the source are linearly stable when $\sigma_i \leqslant 0$ for $i = 1, 2, 3$ and these inequalities are satisfied within regions of the (S, S_f) plane that we label as $R1$ and $R2$, as depicted in figure 1. Recall that we anticipate that $S_f \geqslant 1$ and so we focus on region $R1$, although the other region of stability, $R2$, is included for completeness. In particular, region $R1$ is given by

$$1 \leqslant S_f \leqslant \frac{2S(5S + 1) + (10S + 1)\sqrt{S^2 - S}}{15S + 1}. \tag{3.15}$$

Notably, when $S_f = 1$, the steady plume is linearly stable when

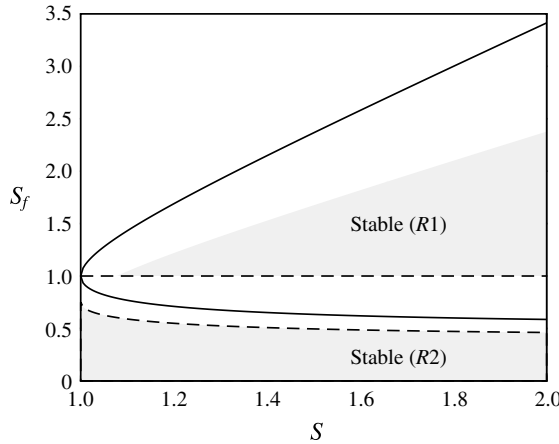$$S \geqslant \frac{1}{2} + \frac{\sqrt{3}}{3}. \tag{3.16}$$

FIGURE 1. The regions $R1$ and $R2$ within the plane of shape factors, (S, S_f), for which the steady line plume solution (2.13) is stable to harmonic disturbances to the source (shaded region, bordered by dashed lines). Also plotted are the parameter values for which the governing system of equations are ill-posed (solid lines).

(*cf.* Woodhouse *et al.* (2016) for axisymmetric plumes). Note further that if the shape factors for the momentum and buoyancy fluxes are equal ($S = S_f$), then linear stability requires

$$S \geqslant \frac{1}{2} + \frac{3\sqrt{5}}{10}. \tag{3.17}$$

We observed above that particular values of the shape factors require special attention in order to determine their linear stability. First we examine the linear stability when $S = 1$ and $S_f \neq 1$. In this situation the eigenvalues are degenerate, $\lambda_2 = \lambda_3 = 1$, and so the system admits the following two eigenvalues and sets of vectors at leading order,

$$\lambda_1 = 1/S_f, \quad \boldsymbol{e}_{L1}^T = (1, -1, -1 + 1/S_f), \quad \boldsymbol{e}_{R1}^T = (0, 0, 1), \tag{3.18a-c}$$

$$\lambda_2 = 1, \quad \boldsymbol{e}_{L2}^T = (1, -1, 0), \quad \boldsymbol{e}_{R2}^T = (1, 1, 0). \tag{3.19a-c}$$

At $O(1/\xi)$, the solvability criterion (3.12) determines the growth rate $\sigma_1 = 1/(S_f - 1)$, but σ_2 is not determined because all the terms in (3.12) vanish. Thus we must proceed to higher order, for which we first find that $\boldsymbol{\psi}_1^T = \mathrm{i}(\sigma_2 + 1)(1, 0, -S_f/(1 - S_f))$. Then at $O(1/\xi^2)$, the solvability condition is given by

$$\boldsymbol{e}_{L1}^T((\sigma_2 - 1)\boldsymbol{A} + \boldsymbol{C})\boldsymbol{\psi}_1 = 0, \tag{3.20}$$

and this leads to $\sigma_2 = -1$ and $\sigma_2 = (2S_f - 1)/(1 - S_f)$. Thus when $S = 1$, linear stability requires that $S_f \leqslant 1/2$.

When $S_f = S \pm \sqrt{S^2 - S}$, we need a different approach, because the eigenspace is degenerate (due to the coincidence of two of the characteristic curves) and the consequential singularities are not removable. In this case we construct the following series for $\phi(\xi)$ and $\boldsymbol{\psi}(x)$ when $\xi \gg 1$,

$$\phi = -\mathrm{i}\lambda\xi + \nu\xi^{1/2} + \sigma \log \xi + \cdots \quad \text{and} \quad \boldsymbol{\psi} = \boldsymbol{\psi}_0 + \frac{1}{\xi^{1/2}}\boldsymbol{\psi}_a + \frac{1}{\xi}\boldsymbol{\psi}_1 + \cdots. \tag{3.21a,b}$$

At leading order, we find two distinct eigenvalues, each of which have left and right eigenvectors. If we suppose that $\lambda_1 = \lambda_2$ (see (3.7) and (3.9)) then the eigenvectors associated with this eigenvalue are

$$\boldsymbol{e}_{L1}^T = (-S/S_f, 1, 0) \quad \text{and} \quad \boldsymbol{e}_{R1}^T = (0, 0, 1), \tag{3.22a,b}$$

while the eigenvectors associated with eigenvalues λ_3 are still given by (3.9). We substitute the revised series (3.21) into (3.3) and equate successive powers of $\xi^{-1/2}$. At $O(\xi^{-1/2})$ we find that

$$\boldsymbol{\psi}_a^T = \frac{i\nu S_f}{2(1 - S_f)}(1, S_f, 0). \tag{3.23}$$

The solvability criterion at $O(\xi^{-1})$ leads to

$$\boldsymbol{e}_{L1}^T(\sigma \boldsymbol{A} + \boldsymbol{C})\boldsymbol{e}_{R1} + \tfrac{1}{2}\nu \boldsymbol{e}_{L1}^T \boldsymbol{C} \boldsymbol{\psi}_a = 0, \tag{3.24}$$

and this implies that $\nu^2 = 2i/S_f$. Furthermore we find that

$$\boldsymbol{\psi}_1^T = -\frac{iS_f}{2(S_f - 1)^2}(\sigma(S_f - 1) - 1, S_f(\sigma(S_f - 1) + S_f - 2), 0). \tag{3.25}$$

Finally we apply the solvability criterion at $O(\xi^{-3/2})$ to deduce

$$\sigma = -\frac{(4S_f^2 - 3S_f - 2)}{8S_f(S_f - 1)}. \tag{3.26}$$

There is one final important special case to consider, namely when both shape factors are set equal to unity, $S = S_f = 1$, a case that can only hold if the plume adopts piecewise constant velocity and density profiles (i.e. 'top-hat' profiles). In this situation there is only one eigenvalue, $\lambda = 1$ and a degenerate eigenspace. There are two independent left and right eigenvectors associated with this single eigenvalue, so we write

$$\boldsymbol{e}_R^T = (1, 1, a) \quad \text{and} \quad \boldsymbol{e}_L^T = (1 + b, -1, -b), \tag{3.27a,b}$$

where a and b are real-valued. We substitute the series (3.21) into (3.3) and equate in successive powers of $O(\xi^{-1/2})$. At each order of which we apply a solvability condition which must hold for all values of a and b, in addition to calculating the appropriate terms in the expansion of $\boldsymbol{\psi}$. Thus we find that

$$\boldsymbol{\psi}_0 = (1, 1, 1), \quad \boldsymbol{\psi}_a = (i\nu/2, 0, 0) \quad \text{and} \quad \boldsymbol{\psi}_1 = (i(\sigma + 1), 0, -i), \tag{3.28a-c}$$

while the solvability conditions imply

$$\nu^2 = 4i \quad \text{and} \quad \sigma = -5/4. \tag{3.29a,b}$$

The implication of these last two derivations and results (3.26) and (3.29) for the special cases $S_f = S \pm \sqrt{S^2 - S}$ and $S = S_f = 1$ are that small disturbances grow exponentially in the far field: when $S = S_f = 1$ the growth of the dependent variables is proportional to $\exp(\sqrt{2\xi})/\xi^{5/4}$, while when $S_f = S \pm \sqrt{S^2 - S}$ and $S \neq 1$, the growth

is proportional to $\exp(\sqrt{\xi/S_f})\xi^\sigma$ (where σ is given by (3.26)). Reinserting the dimensional dependences for a harmonic disturbance of angular frequency ω, we find that the exponent of the exponential growth of the perturbation is proportional to $\omega^{1/2}$ and thus disturbances of high frequency grow with a larger exponent. Consequently, since a general disturbance, such as an instantaneous change of source buoyancy flux (see § 4), will feature all frequencies, the model is ill-posed because it will not be possible to resolve their dependence.

We may then summarise our findings from this investigation. If both shape factors are set to unity then the system of equations for the line plume are ill-posed and moreover ill-posedness remains if two of the characteristic curves coincide (so that $S_f = S \pm \sqrt{S^2 - S}$). When the system is well-posed, there is the further constraint of linear stability, which here we define as bounded spatial evolution in the far field. This limits possible values of the shape factors S and S_f to lie within the regime depicted in figure 1 for which none of the growth rates are positive. In particular when $S_f = 1$, the models are linearly unstable when $1 < S < S_* \equiv 1/2 + \sqrt{3}/3$ and linearly stable when $S > S_*$.

To confirm these predictions of linear stability we compute numerical solutions to the nonlinear governing equations (3.2) driven by a harmonic disturbance of small amplitude to the source condition. Our numerical method uses the central upwind scheme of Kurganov, Noelle & Petrova (2001) with a third-order total variation diminishing Runge–Kutta time stepping scheme and an adaptive time step that ensures that the Courant–Friedrichs–Lewy (CFL) number remains fixed at $1/2$ to maintain numerical stability (see Woodhouse *et al.* (2016) for the application of this technique to axisymmetric plumes). We found that some numerical solutions required a relatively high spatial resolution to yield accurate results over our relatively large domains, but the run times are not excessively long. (For example, with a spatial resolution of 10^{-1}, a domain size of 10^3 and runs over 10^3 dimensionless time units, the numerical integration took 10 hours on a single processor desktop machine.)

We compare the predictions of linear stability to the numerical results by initiating the variables in the steady state, $\boldsymbol{q}(\xi, 0) = (1, 1, 1)$, together with a small harmonic disturbance at the origin, $\boldsymbol{q}(0, \tau) = (1, 1, 1 + \epsilon e^{i\tau})$. The magnitude of the perturbation ϵ, is chosen to be 10^{-2} or 10^{-3} so that the perturbations to the dependent fields remain sufficiently small throughout the entire domain and the dynamics are accurately captured by the linearised governing equations for which we have analytical predictions of the growth rate (see (3.14)). This perturbation is initiated at $\tau = 0$ and we compute over sufficient times to ensure that the higher harmonic transients associated with the initiation are advected out of the region of interest. We choose various values of the shape factors to illustrate the stability properties. First we examine $S_f = 1$ and various values of S (figure 2); we observe that the largest far-field growth rate, σ_3 in this case, accurately captures the numerical results for both an unstable value ($S = 1.05$) and for two stable values ($S = 1.1$ and $S = 1.15$).

Next, in figure 3 we compare the far-field growth rates for the situation in which the two shape factors are equal ($S = S_f$). In this figure we show results for unstable parameter values ($S = S_f = 1.1$) and for stable values ($S = S_f = 1.2$), and again we observe that the theoretical analysis accurately captures the far-field growth rates. We also present brief numerical evidence to illustrate the stability boundary in region $R2$ (see figure 3). To this end we examine $(S, S_f) = (1.4, 0.5)$ for which the evolution is linearly stable and $(S, S_f) = (1.5, 0.5)$ for which the evolution is linearly unstable. Once more we find that the computationally determined growth/decay rates in the far field are accurately matched by the theoretical analysis.
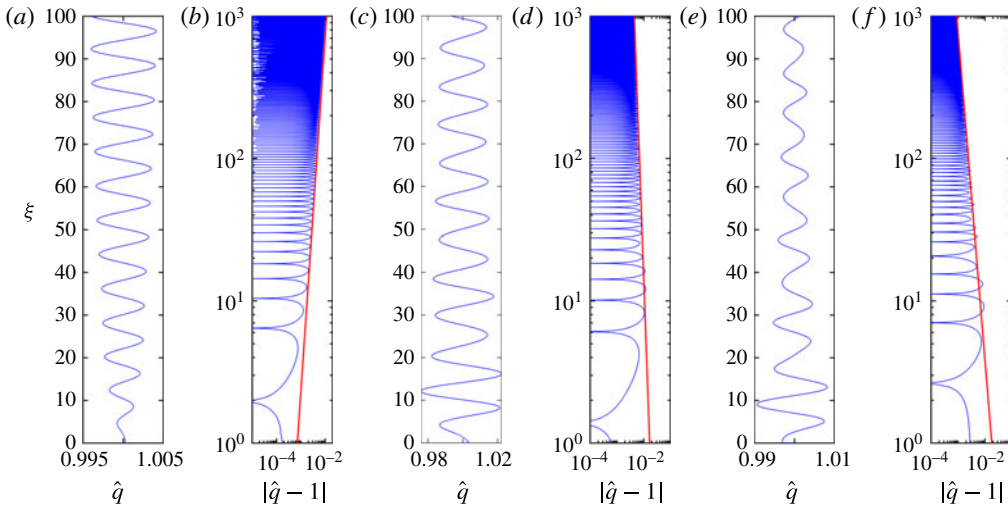
FIGURE 2. (Colour online) The rescaled volume flux per unit width, $\hat{q}(\xi, \tau)$, as a function of dimensionless distance from source, ξ, for the perturbed boundary condition $\boldsymbol{q}(0, \tau) = (1, 1, 1 + \epsilon e^{i\tau})$ and various values of the shape factor, S, while $S_f = 1$ in each case: (*a,b*) $\tau = 790$ and $S = 1.05$; (*c,d*) $\tau = 699$ and $S = 1.1$; (*e,f*) $\tau = 640$ and $S = 1.15$. Also plotted in (*b*), (*d*) and (*f*) are the theoretically predicted growth/decay rates.

Finally we examine the special case of $S = 1$. In this situation the governing system of partial differential equations is parabolic and exhibits just two independent sets of characteristic curves. In this case, it is simple to derive analytical expressions for the perturbed variables (see appendix B), which provide the complete linearised solutions and which confirm the far-field dependence; in particular it is demonstrated that the linearised solutions only decay in the far field if $S_f < 1/2$ as determined above (see (3.20)). We also note that since the system is parabolic, we may no longer independently specify the values of all of the dependent variables at the source and that the numerical solution of the governing equations requires a different strategy since the problem is no longer hyperbolic. Henceforth we do not consider this special case further and restrict our attention to pairs of values of the shape factors drawn from the stable regions $R1$ and $R2$ as depicted in figure 1.

4. Plume dynamics in response to an abrupt change in buoyancy flux

We now consider the unsteady, nonlinear evolution that occurs when the source buoyancy flux per unit width changes abruptly from f_0 to f_1 at $\tau = 0$. We find that the ratio of the old to the new buoyancy flux, $\mathcal{F} = f_0/f_1$, is an important parameter in the dynamic response of the plume to the abrupt change in the source condition. Prior to the change in source conditions, the plume is in a steady state given by (2.13) with f_1 replaced by f_0. After the new buoyancy flux has been imposed for sufficient time, the line plume will adjust to a new steady state given by (2.13). In this calculation we analyse the unsteady adjustment between these two steady states, which we show corresponds to a disturbance that is advected through the domain from the source. Furthermore we show that this adjustment occurs in a self-similar way and we construct the underlying similarity solutions, which we demonstrate depend on the ratio of the buoyancy fluxes, $\mathcal{F}$, and the shape factors, S and S_f.
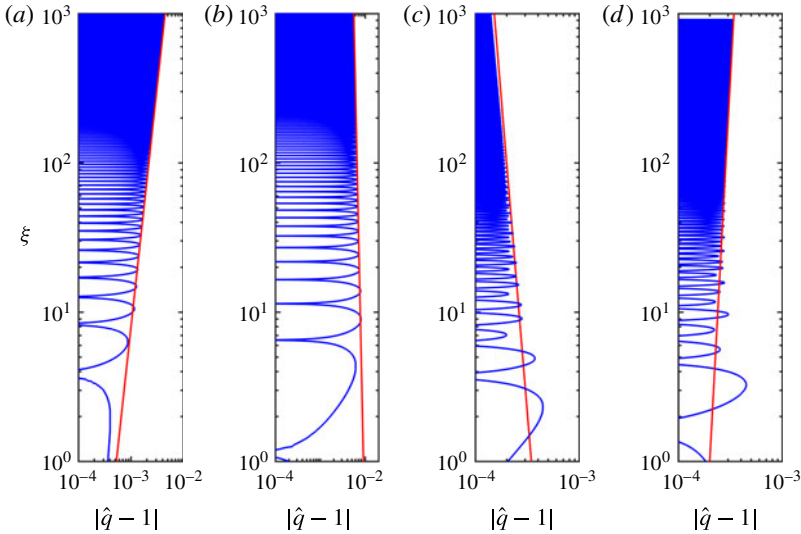
FIGURE 3. (Colour online) The rescaled flux per unit width, $\hat{q}(\xi, \tau)$, as a function of dimensionless distance from source, ξ, for the perturbed boundary condition $q(0, \tau) = (1, 1, 1 + \epsilon e^{i\tau})$ and various values of the shape factors: (a) $\tau = 700$ and $S = S_f = 1.1$; (b) $\tau = 592$ and $S = S_f = 1.2$; (c) $\tau = 620$, $S = 1.4$ and $S_f = 0.5$; (d) $\tau = 1450$, $S = 1.5$ and $S_f = 0.5$. Also plotted in (a–d) are the theoretically predicted growth/decay rates.

First we show the results from direct numerical integration of the governing equations (3.2) in a regime for which the model is well-posed and linearly stable (see §3 and figure 2): we choose shape factors $(S, S_f) = (1.1, 1)$ and examine the response to different changes in the buoyancy flux per unit width. In all the cases plotted in figure 4, namely $\mathcal{F} = 0.1, 2$ and 10, we see that the solution transitions from one steady state to another through the unsteady propagation of a growing region through the domain, and that the half-width of the line plume is independent of buoyancy flux when it has attained the steady state. We observe that when the source buoyancy flux is increased ($\mathcal{F} < 1$), the plume width increases throughout the transient region and that a shock emerges at the leading edge (figure 4a). Conversely, for reductions in buoyancy flux ($\mathcal{F} > 1$) that are relatively small, the plume narrows throughout the transient region, the leading and trailing edges connect continuously to the steady state (figure 4b). Furthermore, when the reduction in the buoyancy flux becomes sufficiently large, there is an internal jump in the flow fields (compare the results for $\mathcal{F} = 2$ and $\mathcal{F} = 10$, figures 4(b) and 4(c) respectively). We now analyse this motion in terms of similarity solutions and show how the adjustment from one steady state to another and the propagation of the transient region through the domain occur in a self-similar way.

A line plume generated by an instantaneous change of buoyancy flux at the source has no externally imposed length or time scales. We therefore expect the adjustment to occur as a similarity solution in which vertical length scales are geared to the distance travelled by the buoyancy-induced motion. (In dimensional terms, $z \sim f_1^{1/3} t$.) Thus we seek solution to (3.2) for q as functions of $y = \xi/\tau$. In fact it is convenient to seek solutions in terms of $(B(y), Q(y), G(y)) = (\hat{b}, \hat{q}/y, \hat{g}/y^2)$ and under these definitions,
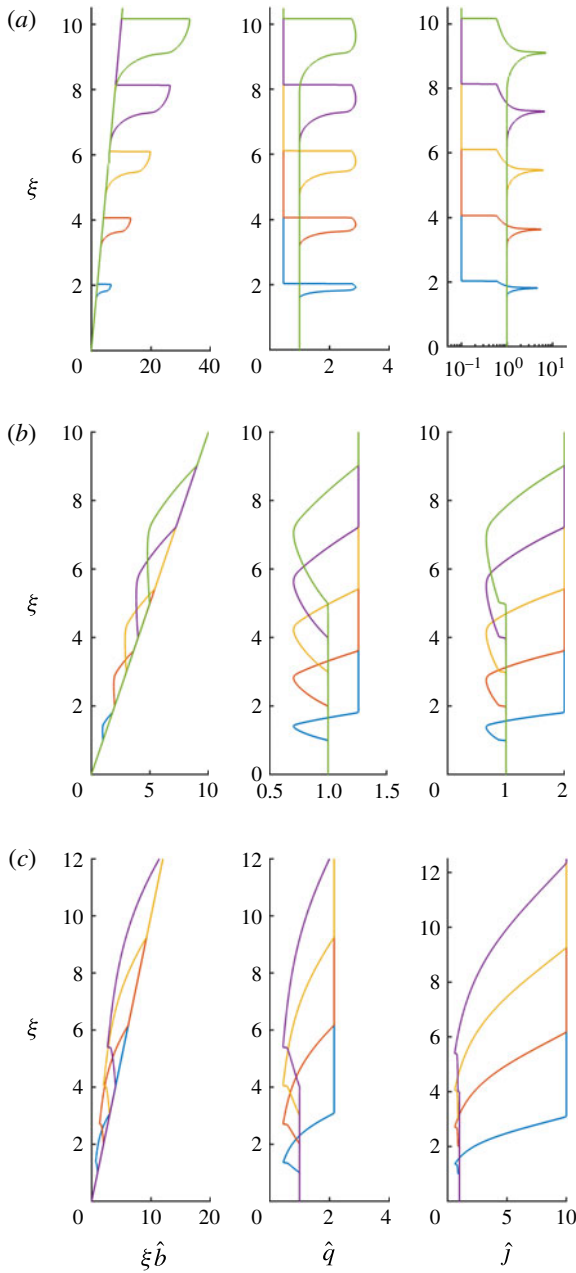
FIGURE 4. (Colour online) The rescaled width $\xi\hat{b}(\xi)$, volume flux $\hat{q}(\xi)$ and buoyancy flux $\hat{j}(\xi)$ as functions of the dimensionless distance from source, ξ, for various ratios of the source buoyancy flux, $\mathcal{F}$ imposed upon the system at $\tau = 0$. (a) $\mathcal{F} = 0.1$ and $\tau = 2, 4, 6, 8, 10$; (b) $\mathcal{F} = 2$ and $\tau = 2, 4, 6, 8, 10$; (c) $\mathcal{F} = 10$ and $\tau = 1, 2, 3, 4$. In all computations, $S = 1.1$ and $S_f = 1$.

we find that the similarity functions satisfy

$$y \begin{pmatrix} -1 & 1 & 0 \\ -SQ^2/B^2 & 2SQ/B - 1 & 0 \\ -S_f GQ/B^2 & S_f G/B & S_f Q/B - 1 \end{pmatrix} \frac{\mathrm{d}}{\mathrm{d}y} \begin{pmatrix} B \\ Q \\ G \end{pmatrix} = \begin{pmatrix} -Q(2 - 1/B) \\ S(G - 3Q^2/B) + Q \\ G(2 - 3S_f Q/B) \end{pmatrix}. \quad (4.1)$$

We denote $\boldsymbol{Q}^T = (B, Q, G)$ and symbolically write this equation as $y\boldsymbol{D}\,\mathrm{d}\boldsymbol{Q}/\mathrm{d}y = \boldsymbol{b}$ for matrix $\boldsymbol{D}$ and vector $\boldsymbol{b}$, which are functions of $\boldsymbol{Q}$. The similarity equations and boundary conditions feature only the shape factors, S and S_f, and the buoyancy ratio $\mathcal{F}$.

We note that this system (4.1) admits a simple solution in which all of the dependent fields are constant $(B, Q, G) = (1/2, \, 1/(3S_f), \, (2S - S_f)/(3SS_f^2))$. This solution corresponds to a 'separable' similarity solution, an analogous form of which has been identified for axisymmetric plumes (Scase *et al.* 2006; Craske & van Reeuwijk 2016) and line jets (Craske 2017). However, as will be shown below, this simple solution does not satisfy the boundary conditions associated with an instantaneous change in buoyancy flux and so does not represent the ensuing dynamics. Instead, one must compute a spatially varying solution for $\boldsymbol{Q}$ in order to establish the similarity solution.

In the far field, $y \gg 1$, the similarity solution adopts the steady state associated with the old buoyancy flux. Thus

$$(B, Q, G) \to (1, \mathcal{F}^{1/3}/y, \mathcal{F}^{2/3}/y^2) \quad \text{as } y \to \infty. \quad (4.2)$$

Conversely, at the origin the solution adopts the steady state associated with the new buoyancy flux. Thus

$$(B, Q, G) \to (1, 1/y, 1/y^2) \quad \text{as } y \to 0. \quad (4.3)$$

Both the behaviour in the far field (4.2) and near field (4.3) are, by construction, exact solutions to the similarity equations (4.1). More general solutions can only diverge from these exact forms at either discontinuities ('shocks') or at locations at which the matrix $\boldsymbol{D}$ is singular. In terms of the dimensionless variables, if a shock is located at $\xi_s = y_s \tau$, then denoting $W = Q/B$, we find that the jump conditions (2.12) are given by

$$[B(W - 1)]_{y_s^-}^{y_s^+} = 0, \quad [BW(SW - 1)]_{y_s^-}^{y_s^+} = 0 \quad \text{and} \quad [G(S_f W - 1)]_{y_s^-}^{y_s^+} = 0. \quad (4.4a\text{--}c)$$

The matrix $\boldsymbol{D}$ is singular when $W = 1/\mu$, where $\mu = \mu_1 \equiv S_f$ or $\mu = \mu_\pm \equiv S \pm \sqrt{S^2 - S}$. From the near-source solution (4.3), we thus deduce that the location closest to the source at which the solution can transition from its form with the new buoyancy flux is $y_l = \mu_-$ (provided $S - \sqrt{S^2 - S} < S_f$), while the location furthest from the source beyond which the solution has adjusted completely to the old buoyancy flux is $y_u = \mathcal{F}^{1/3}\mu_+$ (provided $\mathcal{F}^{1/3}(S + \sqrt{S^2 - S}) > S_f$). These correspond, respectively, to the slowest moving characteristic associated with the new buoyancy flux and the fastest characteristic associated with the old flux, originating from the source.

To integrate the similarity equations (4.1), we must numerically compute the solutions close to singular points of the governing system and it is valuable to use local series expansions for the dependent variables so that the numerical integration may avoid passing through these points. Thus we analyse the behaviour local to $y = y_c$ at which the dependent variables $\boldsymbol{Q} = \boldsymbol{Q}_0 \equiv (B_0, B_0/\hat{\mu}, G_0)$, where $\hat{\mu} = \mu_\pm$ and B_0 and G_0 are as yet undetermined. (We note that the expansion for the singular points at which $\hat{\mu} = \mu_1$ takes a different form and must be treated separately.)

We introduce the following expansion series for the dependent variables and functions of it,

$$(\mathbf{Q}, \mathbf{D}, \mathbf{b}) = (\mathbf{Q}_0, \mathbf{D}_0, \mathbf{b}_0) + (y - y_c)(\mathbf{Q}_1, \mathbf{D}_1, \mathbf{b}_1) + (y - y_c)^\beta (\mathbf{Q}_\beta, \mathbf{D}_\beta, \mathbf{b}_\beta) + \cdots, \quad (4.5)$$

where $\beta > 0$ is not an integer. We substitute (4.5) into (4.1) and equate in successive powers of $(y - y_c)$. At $O(1)$ we find that

$$y_c \mathbf{D}_0 \mathbf{Q}_1 = \mathbf{b}_0. \qquad (4.6)$$

The matrix $\mathbf{D}_0$ is singular and admits vectors $\mathbf{r}^T = (1, 1, S_f G_0 (1 - \mu_\pm)/(B_0 (S_f - \mu_\pm)))$ and $\mathbf{l}^T = (1, 1 - 2\mu_\pm, 0)$ such that $\mathbf{D}_0 \mathbf{r} = 0$ and $\mathbf{l}^T \mathbf{D}_0 = 0$. The solvability condition is $\mathbf{l}^T \mathbf{b}_0 = 0$ and this implies that

$$G_0 = \frac{1 + (\mu_\pm - 1)B_0}{\mu_\pm^3}. \qquad (4.7)$$

The solution for $\mathbf{Q}_1$ is then given by

$$\mathbf{Q}_1^T = \left(0, \frac{1 - 2B_0}{y_c \mu_\pm}, -\frac{(S_f - \mu_\pm(2 - S_f))B_0 - (2\mu_\pm^2 - (2 + S_f)\mu_\pm + S_f)B_0^2)}{y_c \mu_\pm^3 B_0 (S_f - \mu_\pm)} \right) + K \mathbf{r}^T, \qquad (4.8)$$

where K is an as yet undetermined constant. At $O(y - y_c)$ we enforce a further solvability condition and this yields

$$y_c \mathbf{l}^T \mathbf{D}_1 \mathbf{Q}_1 = \mathbf{l}_1^T \mathbf{b}_1, \qquad (4.9)$$

which leads to two solutions for the constant K, given by

$$K_1 = \frac{B_0 - 1}{y_c(\mu_\pm - 1)} \quad \text{and} \quad K_2 = \frac{B_0(S_f \mu_\pm - 2\mu_\pm^2 + S_f) + 2\mu_\pm^2 - (2S_f - 1)\mu_\pm - 2S_f}{2y_c \mu_\pm(\mu_\pm - 1)(S_f - \mu_\pm)}. \qquad (4.10a,b)$$

Next we consider the non-integer powers: at $O((y - y_c)^{\beta - 1})$, we find $\beta y_c \mathbf{D}_0 \mathbf{Q}_\beta = 0$, which has solution $\mathbf{Q}_\beta = K_\beta \mathbf{r}$, where K_β is a constant. At $O((y - y_c)^\beta)$, we find that

$$y_c \mathbf{l}^T (\mathbf{D}_\beta \mathbf{Q}_1 + \beta \mathbf{D}_1 \mathbf{Q}_\beta) = \mathbf{l}^T \mathbf{b}_\beta. \qquad (4.11)$$

On substituting for each of the values of K (see (4.8) and (4.10)), we find two values for β (denoted β_1 and β_2), given by

$$\beta_1 = \frac{1}{\beta_2} = \frac{B_0(3S_f \mu_\pm - 2\mu_\pm^2 - S_f) + 2S_f - \mu_\pm}{2B_0 \mu_\pm(S_f - \mu_\pm)}. \qquad (4.12)$$

The constant K_β remains undetermined and may be varied to generate different admissible solutions. The power series expansion in integer powers may be straightforwardly continued to higher powers if required, which leads to algebraically lengthy expressions that are conveniently handled using computer algebra.

Using the same methodology we may examine the behaviour close to a point $y = y_c$ at which $W(y_c) = 1/\mu_1$ (and $\mu_1 = S_f$). We seek expansions for the dependent variables

close to the location and find that

$$
\begin{pmatrix} B \\ Q \\ G \end{pmatrix} = \begin{pmatrix} B_0 \\ \dfrac{B_0}{S_f} \\ \dfrac{B_0 S_f (S-1) + (S_f - S)}{S_f^2 S (S_f - 1)} \end{pmatrix} + \frac{(y - y_c)}{y_c (S_f - 1)} \begin{pmatrix} B_0 - 1 \\ -\dfrac{(B_0(S_f - 2) + 1)}{S_f} \\ -\dfrac{2(B_0 S_f (S-1) - S_f + S)}{(S_f^2 S)} \end{pmatrix}
$$

$$
+ K_\beta (y - y_c)^\beta \begin{pmatrix} 0 \\ 0 \\ 1 \end{pmatrix} + \cdots, \tag{4.13}
$$

where the exponent is given by

$$
\beta = \frac{B_0 S_f (S-1) + S_f - S}{B_0 (S(S-1) - (S - S_f)^2)}. \tag{4.14}
$$

It is notable that the leading-order term for G in the expansion (4.13) becomes unbounded at $S_f = 1$ because at that value of the shape factor, discontinuities in this field are advected with the local velocity field (i.e. a contact discontinuity, as noted in § 2).

We now construct the similarity solutions and demonstrate that they generate the nonlinear evolution computed directly from the governing partial differential equations. We illustrate three separate forms of solutions by first analysing $S_f = 1$, $S = 1.1$ and various values of the changes in buoyancy flux, $\mathcal{F}$. These reveal the generic forms of the solutions if $|S_f - S| < \sqrt{S^2 - S}$ and the shape factors are drawn from region $R1$ (see figure 1). In appendix D we analyse the nonlinear motion when the shape factors are drawn from region $R2$ (figure 1). For these cases we find some additional features in the motion that arise due to an instantaneous change in buoyancy flux and we also construct the underlying similarity solutions (appendix D). In the results that follow (see figures 5, 7 and 10), we demonstrate that the solutions computed through the direct numerical integration of the governing equations (3.2) are indistinguishable from the similarity solutions that are computed using the methods described below.

4.1. *Increase in buoyancy flux: $\mathcal{F} < 1$*

When there is an instantaneous increase in buoyancy flux at the source, the unsteady pulse that propagates through the domain features a shock at its leading edge ($y = y_s$), at which the solution jumps from a faster moving state to the original buoyancy flux. The trailing edge corresponds to the slowest moving characteristic associated with the new flux ($y = y_l$) and in between there exists a location ($y = y_*$) at which the system is singular ($W = 1$). Our method of constructing the solution numerically is as follows: we form a local series expansion for $|y - y_l| \ll 1$, which entails the undetermined constant, K_β, and given this value, we integrate the equations until $y = y_{*1}$ at which $W = 1/S_f = 1$ and $B = B_{*1}$. We also choose a location for the shock at the leading edge, y_s, and using the shock conditions (4.4), integrate backwards to $y = y_{*2}$ at which $W = 1$ and $B = B_{*2}$. We then adjust K_β and y_s until $y_{*1} = y_{*2}$ and $B_{*1} = B_{*2}$. The solution is plotted in figure 5(*a*) for $\mathcal{F} = 0.1$, in which we see that the plume broadens as it adjusts from the old steady state to the new and features the shock at its leading edge. We also find that as $\mathcal{F}$ is decreased, the width of the transition zone also decreases.
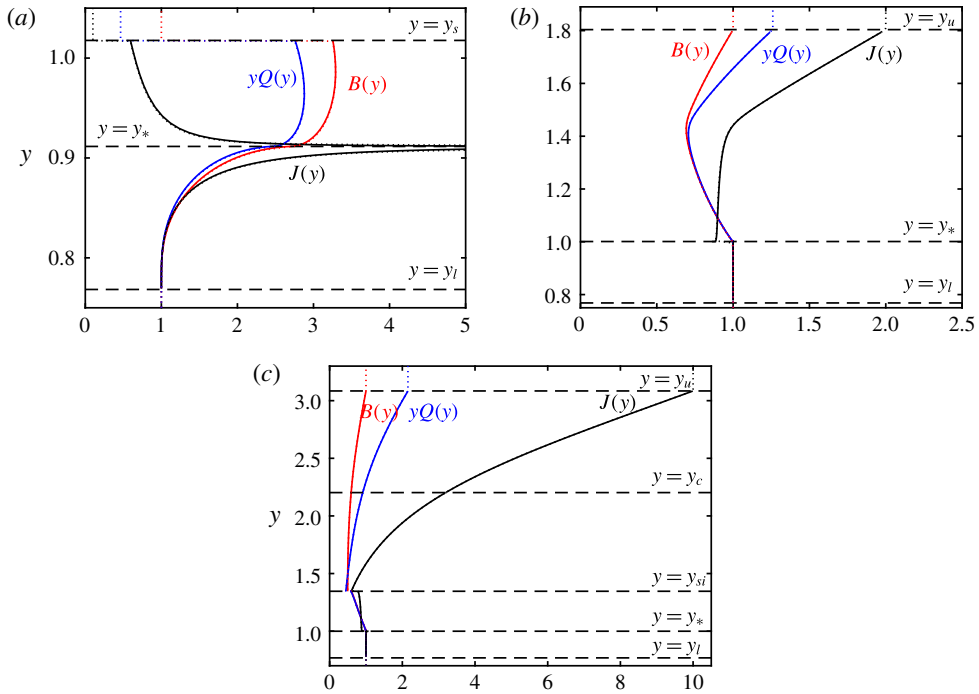
FIGURE 5. (Colour online) (*a–c*) The similarity solutions for the width $B(y)$, volume flux $yQ(y)$ and buoyancy flux $J(y) = y^3 G(y)Q(y)/B(y) = \hat{j}$, for a line plume in response to an instantaneous change in source strength as functions of the similarity variable y (solid lines) and their evaluation from direct numerical integration of (3.2) (dotted lines) for (*a*) $\mathcal{F} = 10$, (*b*) $\mathcal{F} = 0.5$, (*c*) $\mathcal{F} = 0.1$. In this case $S = 1.1$ and $S_f = 1$. Also plotted are various important locations within the solution (y_l, y_*, y_{si}, y_c, y_s and y_u). Note that the similarity solution and numerical integration are virtually indistinguishable.

4.2. *Weak decreases in buoyancy flux: $1 < \mathcal{F} < \mathcal{F}_m(S)$ when $S < 9/8$*

When the buoyancy flux at the source instantaneously decreases ($\mathcal{F} > 1$), then the leading edge of the region within which the solution transitions from the old to the new flux is located at $y = y_u$, corresponding to the fastest moving characteristic associated with the old flux originating from the source at $\tau = 0$. Furthermore the solution is continuous at its leading edge. The transient zone then lies between y_l and y_u. We compute the similarity solution numerically by integrating separately from y_l and y_u towards locations at which $W = 1$. These numerical solutions are initiated by using the series expansions, each of which feature an undetermined constant multiplying the terms with non-integer powers. We adjust the constants until we find a solution for $W = 1$ at $y = y_*$ and B is continuous. We note from figure 5(*b*) for $\mathcal{F} = 0.5$ that the plume narrows and accelerates as the buoyancy flux increases from its near-source value to its value in the far field.

4.3. *Strong decreases in buoyancy flux: $\mathcal{F}_m(S) < \mathcal{F}$ and $S < 9/8$*

When the decrease in buoyancy flux at the source is sufficiently large and $S < 9/8$, the similarity solution attains the singular value of $W = 1/\mu_+$ both at the farmost extent of the transition zone ($y = y_u$), but also at some interior location ($y = y_c$) at which
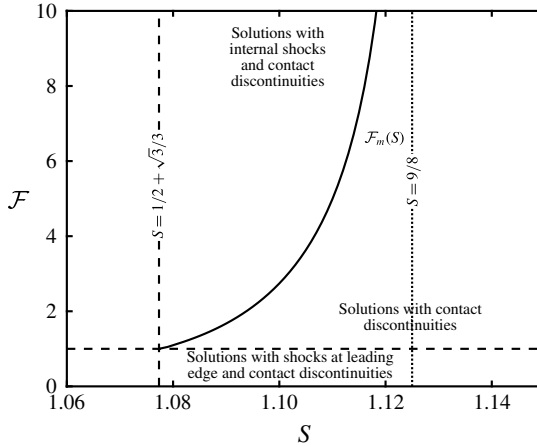
FIGURE 6. The regimes of similarity solutions in the $(S, \mathcal{F})$ plane for $S_f = 1$. Also plotted is the buoyancy flux ratio at source, at which internal shocks first appear, $\mathcal{F}_m$, as a function of the shape factor S (solid line). The value $S = 1/2 + \sqrt{3}/3$ is plotted (dashed line) and this corresponds to the threshold for linearly stable solutions, while solutions with internal shocks are not found for $S > 9/8$.

the dependent variables are continuous. However, complete flow solutions can only be constructed consistently by introducing an internal shock at $y = y_{si}$ ($y_{si} < y_c$), at which W and B are discontinuous. The solutions also pass through the critical point $y = y_*$ ($y_* < y_{si}$) at which $W = 1$ and B is continuous before connecting with the solutions emanating from y_l.

The solution is most easily constructed numerically as follows. Values of four variables are assumed, namely the location y_c and $B(y_c) = B_0$ at which $W(y_c) = 1/\mu_+$, the location of the internal shock, y_{si}, and the value of the constant, K_β, multiplying the non-integer powers in the series expansion close to y_l. Given these choices, we integrate from $y = y_c$ to $y = y_u$, using series expansions to initiate the numerical integration and evaluate $N_1 = B(y_u) - 1$ and $N_2 = G(y_u) - \mathcal{F}^{2/3}/y_u^2$. We also integrate from $y = y_c$ to $y = y_{si}$ at which point we apply the shock conditions to evaluate the jump in values of B and W. We then integrate to $y = y_{*2}$ at which $W(y_{*2}) = 1$ and $B(y_{*2}) = B_{*2}$. We also integrate from $y = y_l$ to $y = y_{*1}$ at which $W(y_{*1}) = 1$ and $B(y_{*1}) = B_{*2}$, and then evaluate $N_3 = y_{*1} - y_{*2}$ and $N_4 = B_{*1} - B_{*2}$. We iteratively adjust the values of y_c, B_0, y_{si} and K_β until $N_1 = N_2 = N_3 = N_4 = 0$. A typical solution in plotted in figure 5(*c*), in which the narrowing of the plume is evident in addition to the internal shock across which the dependent variables change discontinuously.

The ratio of the buoyancy fluxes at which an internal jump first appears depends upon the shape factor, S and is denoted $\mathcal{F}_m(S)$. When $1 \leqslant \mathcal{F} < \mathcal{F}_m$, solutions without an internal jump are found. Instead, when $\mathcal{F} = \mathcal{F}_m$ the solution exhibits a discontinuous gradient at the internal singular point $y = y_c$ and the series expansion switches from featuring K_2 to K_1 (4.10). In this way, we can evaluate $\mathcal{F}_m$ and it is plotted in figure 6. The limiting case occurs when the gradients of W and B vanish at $y = y_c$, which from (4.8) and (4.10) occurs at $B_0 = 1/2$ and $\mu_+ = 3/2$ (and consequentially $S = 9/8$). Thus we find that only continuous solutions arise for $\mathcal{F} > 1$ when $S > 9/8$. The regimes of solutions are depicted in figure 6.
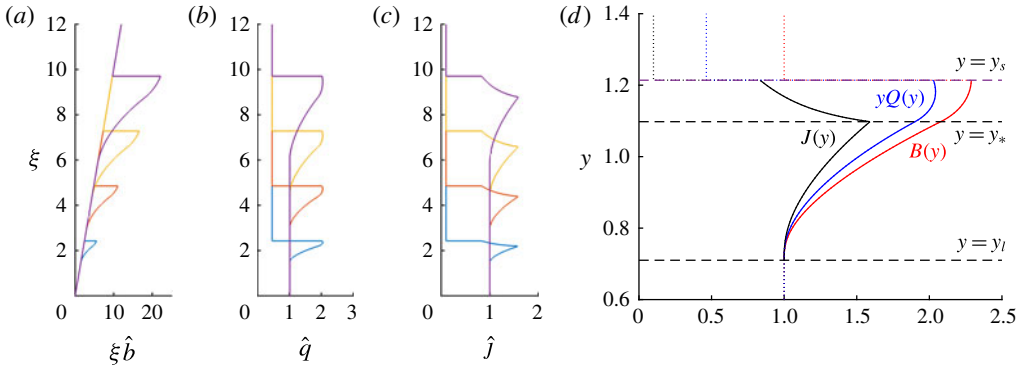
FIGURE 7. (Colour online) (*a–c*) The rescaled width $\xi\hat{b}(\xi)$, volume flux $\hat{q}(\xi)$ and buoyancy flux $\hat{j}(\xi)$ as functions of the dimensionless distance from source, ξ, for an instantaneous increase in the buoyancy flux per unit width at the origin ($\mathcal{F} = 0.1$) at dimensionless times $\tau = 2, 4, 6$ and 8. (*d*) The similarity solution for $B(y)$, $Q(y)$ and $J(y)$ as functions of the similarity variable, y (solid lines), and the results from the direct numerical integration of the governing equations (3.2) (dotted lines). Note that the two solutions are virtually indistinguishable. Also shown are three important locations (y_l, y_{si}, y_s) in the construction of the similarity solution. In these computations, $S = 1.2$ and $S_f = 1.2$.

4.4. *Other similarity solutions*

The similarity solutions that we have constructed in §§ 4.1–4.3 are representative of those found for shape factors drawn from region *R*1 of figure 1. In this subsection we illustrate the results for one additional pair of shape factors drawn from this region, namely $S = S_f = 1.2$. For these values there is no longer the possibility of a contact discontinuity since $S_f \neq 1$ (see (2.12) and (4.4)) and we find that at locations where $W = 1/S_f$, the similarity solution for the reduced gravity remains finite (see (4.13)).

We compute the response of the line plume to an instantaneous increase in the source buoyancy flux ($\mathcal{F} = 0.1$) (figure 7*a–c*). The dynamics are broadly similar to when $S_f = 1$ (figure 4*a*) and show that the transient response is led by a shock at the leading edge, where the dependent variables change discontinuously from the previous steady states. Furthermore the plume broadens as the fluid decelerates from velocities determined by the new buoyancy flux to those set by the previous state. The local buoyancy flux increases before decreasing to match the far field. The main difference that we observe when $S_f > 1$ is that the buoyancy flux increases less and remains finite (see figure 7*c*).

This response is also captured accurately by the corresponding similarity solution (figure 7*d*). We construct it using identical techniques to those described in § 4.1 and we thus determine the solution for $y_l < y < y_s$.

Finally, in appendix D we compute similarity solutions for shape factor drawn from region *R*2 of figure 1. Due to the reordering of the characteristic velocities for values of the shape factors from this region, these similarity solutions feature different phenomena from those reported above but continue to accurately capture direct numerical solutions of the governing equations when the source buoyancy flux is either increased or decreased instantaneously.

5. Summary and conclusions

In this study we have developed a well-posed, integral model for the unsteady motion of line plumes and have demonstrated the need to account for the variation of the vertical velocity and the reduced gravity across the plume, rather than assuming they adopt 'top-hat' distributions. This introduces shape factors, S and S_f, that are related to the variance of the distribution of vertical velocity and the covariance of the distributions of vertical velocity and reduced gravity, respectively. Both shape factors are equal to unity if these fields adopt 'top-hat' profiles and crucially this leads to an ill-posed system of time-dependent equations. Such a system cannot be used for computing temporally varying flows. This result extends to line plumes what has been established for axisymmetric plumes (Scase & Hewitt 2012; Craske & van Reeuwijk 2016; Woodhouse *et al.* 2016). We have also demonstrated that ill-posedness can arise when $S_f = S \pm \sqrt{S^2 - S}$. With the additional constraint of linear stability, which requires perturbations to decay in the far field, we showed that this restricts the admissible values of the shape factors to certain regions of the (S, S_f)-plane (figure 1). We calculated the asymptotic growth/decay rates in the far field in response to a sustained harmonic disturbance to 'pure' plume source conditions and confirmed these predictions by direct numerical integration of the governing system of three partial differential equations that express mass and buoyancy conservation and the balance of vertical momentum. It is interesting to note that these distributions of velocity and reduced gravity, captured here through shape factors, play a significant role in unsteady integral models, but not in the steady states which are essentially determined through dimensional reasoning. We also comment that since these deductions are based upon the far-field behaviour, we anticipate that the results will carry over to the stability of steady states for 'forced' and 'lazy' line plumes in which the source conditions are not in 'pure' plume balance (see van den Bremer & Hunt (2014)). Solutions with such source conditions adjust to solutions generated by 'pure' plume conditions sufficiently far from source and thus the same far-field deductions about linear stability follow (see § 3).

When there is an instantaneous change in the buoyancy flux per unit width at the source, the line plume adjusts from one steady state to another though a transient 'pulse' that advects through the domain. This nonlinear adjustment occurs in a self-similar way. We determined the similarity solutions that underlie this motion; these are functions of the similarity variable for which the vertical length, z, is geared linearly to time, t. Essentially the self-similarity arises because there are no externally imposed length or time scales in the flow, other than the buoyancy flux per unit width at the source. We showed how the nonlinear adjustment is a function of the ratio of the old to new buoyancy fluxes and the shape factors. For instantaneous increases in the buoyancy flux per unit width, we found that the transient response is led by a shock over which the dependent variables are discontinuous. The plume broadens and slows toward the leading edge as the dynamics adjust to meet the previously established steady state. Conversely, for an instantaneous decrease in buoyancy flux per unit width, we found that the plume narrows and accelerates. The similarity solutions feature internal shocks and critical points at which the gradients of dependent variables change discontinuously. We showed that the similarity forms could be computed by integrating the three coupled ordinary differential equations that arise from the governing system and described the numerical strategies required for applying the appropriate boundary conditions for various values of the shape factors and ratio of old to new buoyancy fluxes per unit width at the source.

Models of unsteady line plumes are closely related to their axisymmetric counterparts, although the geometrical change leads to several differences in their behaviour. The integral models for line and axisymmetric plumes both feature two shape factors (cf. Woodhouse *et al.* 2016) and the magnitude of these factors leads to situations in which steady solutions may be linearly stable or unstable, as well as the governing equations exhibiting ill-posedness (Scase & Hewitt 2012). In this study we have analysed variations of both shape factors, adding to the more restrictive study by Woodhouse *et al.* (2016) of axisymmetric plumes, which analysed just the variation of S. Furthermore the thresholds of stability differ in each of the two configurations. For instantaneous changes of the buoyancy flux per unit width at the source, we have shown that the line plumes adjust to the new steady state via similarity solutions. Analogous behaviour was found for axisymmetric plumes (Woodhouse *et al.* 2016), but for line plumes the gearing between temporal and spatial scales, which underpins the self-similarity form, differs from their axisymmetric counterparts.

Measurements of plumes are often used to infer geophysical characteristics of the source. For example, observations of line plumes generated by volcanic activity in submarine (such as lava extrusion during seafloor spreading events which produce hydrothermal plumes in the ocean, e.g. Baker *et al.* (1995)) and subareal (such as fissure eruptions that produce line plumes of volcanic gases and ash, e.g. Glaze, Baloga & Wimert (2011)) settings are used to determine the fluxes of mass and heat from the intruding magmatic source. Arguably the simplest observation to make is to image the visible edge of the plume. Our analysis demonstrates that the development of transient pulses that propagate through the plume preserve information on the unsteady source condition. Thus image sequences, appropriately averaged and analysed, could be utilised to indicate temporal variations in the source conditions and provide greater insight into the geological processes that produce plumes in the oceans and atmosphere of Earth and other planets.

This study has determined the conditions required to produce well-posed integral models of line plumes through uniform environments based upon the assumption of a constant entrainment coefficient (Morton *et al.* 1956). Other researchers (e.g. Kaminski *et al.* 2005; Craske & van Reeuwijk 2016) have adopted different closures and while we have examined the linear stability of steady line plumes modelled by extending Craske (2017) to include buoyancy effects (appendix C), it would be interesting to explore more completely the resultant difference in the well-posedness and stability properties for unsteady dynamics and the nonlinear self-similar response. This analysis can be carried out using the same analytical frameworks described above. Moreover it would be interesting to explore these ideas through laboratory experimentation and numerical simulation of the Navier–Stokes equations in this two-dimensional geometry. Future studies could also apply this well-posed model to a range of unsteady applications, including the important situation in which the line plume ascends through a density-stratified environment and intrudes around its neutral buoyancy elevation.

Appendix A. Derivation of governing equations

The equations modelling the evolution of a turbulent line plume in a uniform environment are the two-dimensional versions of the expressions derived in axisymmetric geometry by Woodhouse *et al.* (2016). The equations model the evolution of the two-dimensional velocity field $\boldsymbol{u} = (u, w)$ and the reduced gravity g', which in this appendix is linearly related to the field C that gives rise to a density difference,

which is advected by the fluid motion. (For example, the field C could represent the salinity or temperature of the fluids.) The environment through which the plume ascends is of uniform density ρ_0 (and $C = 0$) and the density of the plume is given by $\rho_p = \rho_0 - \Delta\rho C$ so that the reduced gravity is $g' = \Delta\rho C / \rho_0$. The motion is turbulent and we decompose the fields into mean and fluctuating parts, $\boldsymbol{u} = \hat{\boldsymbol{u}} + \boldsymbol{u}'$ and $C = \hat{C} + C'$, in which the caret notation represents the mean and the prime represents the fluctuating part. The temporal averaging is over the relatively rapid time scale of the turbulent eddies so that the mean variables are functions of both space and time. As in § 2, the coordinate axes are aligned so that x is horizontal and z is vertical (and positive upwards).

The fluid motion is incompressible, which is given by

$$\frac{\partial \hat{u}}{\partial x} + \frac{\partial \hat{w}}{\partial z} = 0. \tag{A 1}$$

It is assumed that the plume is relatively narrow so that horizontal length scales of the motion are much smaller than vertical length scales (cf. Linden 2000; Woodhouse *et al.* 2016). As a consequence, we deduce from the horizontal balance of momentum that the horizontal pressure gradient must vanish. Thus, to leading order, the vertical pressure gradient is the same both within the plume and outside it, and given by

$$\frac{\partial \hat{p}}{\partial z} = -\rho_0 g, \tag{A 2}$$

where $\hat{p}$ is the mean pressure and g the magnitude of the gravitational acceleration. Then on the further assumptions that the density differences are sufficiently small for the motion to be in the Boussinesq regime, that viscous processes are negligible and that streamwise fluctuations are much smaller than the mean flow ($\widehat{w'^2} \ll \hat{w}^2$), we find that the vertical balance of momentum is given by

$$\frac{\partial \hat{w}}{\partial t} + \frac{\partial}{\partial x}(\hat{u}\,\hat{w}) + \frac{\partial}{\partial z}(\hat{w}^2) = \frac{\Delta\rho g}{\rho_0}\hat{C} + \frac{\partial \mathcal{J}_m}{\partial x}, \tag{A 3}$$

where $\mathcal{J}_m = -\widehat{u'w'}$ is the Reynolds stress per unit mass. Finally the concentration field satisfies the following equation on the assumptions that molecular diffusivity is negligible and that streamwise transport due to the cross-correlation of the fluctuations is much smaller than the mean transport ($\widehat{w'C'} \ll \hat{w}\hat{C}$),

$$\frac{\partial \hat{C}}{\partial t} + \frac{\partial}{\partial x}(\hat{u}\,\hat{C}) + \frac{\partial}{\partial z}(\hat{w}\hat{C}) = \frac{\partial \mathcal{J}_b}{\partial x}, \tag{A 4}$$

where $\mathcal{J}_b = -\widehat{u'C'}$ is the Reynolds flux. For notational ease, henceforth we drop the carets from the dependent variables, $\hat{u}$, $\hat{w}$ and $\hat{C}$.

We now integrate (A 3) and (A 4) across the half-width of the plume, where the edge of the plume, $x = b(z, t)$ is defined below. This yields

$$\frac{\partial}{\partial t}\int_0^b w\,\mathrm{d}x + \frac{\partial}{\partial z}\int_0^b w^2\,\mathrm{d}x = \frac{\Delta\rho g}{\rho_0}\int_0^b C\,\mathrm{d}x + \mathcal{J}_{mb} + w_b\left(\frac{\partial b}{\partial t} + w_b\frac{\partial b}{\partial z} - u_b\right), \tag{A 5}$$

$$\frac{\partial}{\partial t}\int_0^b C\,\mathrm{d}x + \frac{\partial}{\partial z}\int_0^b wC\,\mathrm{d}x = \mathcal{J}_{bb} + C_b\left(\frac{\partial b}{\partial t} + w_b\frac{\partial b}{\partial z} - u_b\right), \tag{A 6}$$

where the suffix b denotes evaluation of the variable at the edge of the plume $x = b$. In deriving (A 5) and (A 6) we have used the symmetry condition that the horizontal velocity field, u, vanishes at $x = 0$. These equations are the two-dimensional versions of the axisymmetric balances presented by Craske & van Reeuwijk (2016) and Woodhouse *et al.* (2016), although in the latter study, boundary terms evaluated at the edge of the plume were assumed to vanish.

The edge of a plume is defined as the location at which the concentration falls to some fraction, ϵ, of the centreline value; very often $\epsilon = e^{-1}$ (see, for example, Turner (1973), Scase *et al.* (2006)). Thus

$$C(b(z, t), z, t) = \epsilon C_0(z, t), \quad \text{where } C_0 = C(0, z, t), \tag{A 7}$$

and then we find that

$$\left.\frac{\partial C}{\partial t}\right|_b + \left.\frac{\partial C}{\partial x}\right|_b \left(\frac{\partial b}{\partial t} + w_b \frac{\partial b}{\partial z}\right) + w_b \left.\frac{\partial C}{\partial z}\right|_b = \epsilon \left(\frac{\partial C_0}{\partial t} + w(0, z, t)\frac{\partial C_0}{\partial z}\right). \tag{A 8}$$

We use (A 4) evaluated at the centreline and the edge to simplify (A 8) and thus we find

$$\left.\frac{\partial C}{\partial x}\right|_b \left(\frac{\partial b}{\partial t} + w_b \frac{\partial b}{\partial z} - u_b\right) = \epsilon \left.\frac{\partial \mathcal{J}_b}{\partial x}\right|_0 - \left.\frac{\partial \mathcal{J}_b}{\partial x}\right|_b. \tag{A 9}$$

Then, by defining

$$u_e \left.\frac{\partial C}{\partial x}\right|_b = \epsilon \left.\frac{\partial \mathcal{J}_b}{\partial x}\right|_0 - \left.\frac{\partial \mathcal{J}_b}{\partial x}\right|_b, \tag{A 10}$$

we establish the evolution equation for the edge of the plume, namely

$$\frac{\partial b}{\partial t} + w_b \frac{\partial b}{\partial z} = u_b + u_e. \tag{A 11}$$

We note that the edge of the plume does not move as a kinematic interface that is merely advected with the velocity field, because such a condition would require $u_e = 0$. Instead, the turbulent processes lead to an inflow across the interface and increase the volume flux per unit width transported by the plume (Turner 1986). This is the key feature of the dynamics and the entrainment velocity is defined by (A 10). We also note that one could define the edge as the location at which the mean vertical velocity drops to some value of the centreline velocity and then derive an alternative expression to (A 11) for the entrainment velocity based on the Reynolds stress, rather than the Reynolds flux. Immediately from (A 1) and (A 11), we deduce that

$$\frac{\partial b}{\partial t} + \frac{\partial}{\partial z} \int_0^b w \, \mathrm{d}x = u_e. \tag{A 12}$$

We may now complete the width-integrated model by evaluating the terms in (A 5) and (A 6) that are evaluated at the boundary $x = b$ (and denoted with the suffix b). First, however, we comment that these boundary terms are relatively small in magnitude, and this has been used by Craske & van Reeuwijk (2016) and Woodhouse *et al.* (2016) to neglect the equivalent of them from their axisymmetric models. It will be shown though, that in addition to being relatively small in magnitude, they may exactly vanish. If the vertical velocity, concentration and turbulent fluxes are

self-similar across the plume, so that

$$w(x, z, t) = W_0(z, t)h_1(x/b), \quad C(x, z, t) = C_0(z, t)h_2(x/b), \quad (A.13a,b)$$

$$\mathcal{J}_m(x, z, t) = W_0(z, t)^2 h_3(x/b) \quad \text{and} \quad \mathcal{J}_b(x, z, t) = W_0(z, t)C_0(z, t)h_4(x/b), \quad (A.14a,b)$$

where h_i ($i = 1$–4) are the similarity functions and $h_1(0) = h_2(0) = 1$, then we deduce that the entrainment velocity is proportional to the vertical velocity along the symmetry axis, $W(z, t)$, and thus proportional to the mean vertical velocity. In terms of these similarity functions,

$$u_e = W_0 \frac{h_2(1)h_4'(0) - h_4'(1)}{h_2'(1)}. \quad (A\,15)$$

It has been shown experimentally that in a steady state, the mean vertical velocity and reduced gravity within a line plume adopt Gaussian distributions (e.g. Rouse *et al.* 1952; Anwar 1969) and may be written

$$w(x, z, t) = W_0(z, t)\exp(-\mu^2 x^2/b^2), \quad (A\,16)$$
$$g'(x, z, t) = G_0(z, t)\exp(-\gamma^2\mu^2 x^2/b^2), \quad (A\,17)$$

where μ and γ are constants. These empirical results suggest that h_1 and h_2 may be taken as Gaussians and that the concentration threshhold (A 7) $\epsilon = \exp(-\mu^2\gamma^2)$. If we further assume that the similarity functions, h_3 and h_4, are proportional to h_1' and h_2', respectively, which corresponds to an eddy diffusivity closure for the turbulent fluxes, $\mathcal{J}_m$ and $\mathcal{J}_b$, then we find that the boundary term in (A 6), namely $\mathcal{J}_{bb} + C_b u_e$, vanishes. Furthermore the boundary term in (A 5), $\mathcal{J}_{mb} + w_b u_e$, is negligible provided the threshold, ϵ, is small or that γ is close to unity (so that the distributions of vertical velocity and reduced gravity are not too different). In physical terms these results mean that the location of edge of the plume evolves so that the vertical flux concentration field is conserved within the plume. Also it means that the fluid, which is entrained into the plume with small, but non-vanishing, vertical velocity adds to the vertical momentum, but this is balanced by the 'drag' experienced at the edge of the plume. Thus we deduce the three governing equation for line plumes that express conservation of mass (2.1), the balance of streamwise momentum (2.2) and by substituting $C = \rho_0 g'/\Delta\rho$, the conservation of buoyancy (2.3).

A.1. *Alternative unsteady models*

The unsteady formulation presented above utilises a model of the boundary of the plume, $x = b(z, t)$, which does not evolve purely kinematically, but rather evolves due to turbulent fluxes across it that are encompassed in the entrainment velocity, u_e. Other studies have advocated different approaches for modelling the unsteady motion of plumes and jets. For example, Craske (2017), for line jets, and Craske & van Reeuwijk (2016), for axisymmetric jets and plumes, do not model the interface, $b(z, t)$, but rather the volume and specific momentum fluxes per unit width and the buoyancy per unit width associated with the plume, denoted by $\tilde{Q}$, $\tilde{M}$ and $\tilde{G}$, respectively, and defined by

$$\tilde{Q} = \int_0^\infty w \, \mathrm{d}x, \quad \tilde{M} = \int_0^\infty w^2 \, \mathrm{d}x, \quad \text{and} \quad \tilde{G} = \int_0^\infty g' \, \mathrm{d}x. \quad (A\,18a\text{--}c)$$

With this approach, there is no model for the edge of the plume, so the integrals in (A.18) extend to the far field, and no integrated expression for conservation of mass akin to (A 12) is obtained directly. Instead, Craske & van Reeuwijk (2016) and Craske (2017) form an expression for the conseravtion of energy, which for a line plume is given by multiplying (A 3) by $2w$ and integrating to yield

$$\frac{\partial}{\partial t} \int_0^\infty w^2 \, \mathrm{d}x + \frac{\partial}{\partial z} \int_0^\infty w^3 \, \mathrm{d}x = -2 \int_0^\infty \mathcal{J}_m \frac{\partial w}{\partial x} \, \mathrm{d}x + 2 \int_0^\infty \frac{\Delta \rho g}{\rho_0} C w \, \mathrm{d}x. \qquad (\text{A } 19)$$

Craske (2017) presented governing equations for line jets and so the balance of energy did not feature the final term of (A 19). Extending his suggested closure for the turbulent terms to line plumes, we find the following coupled system of governing equations:

$$\frac{\partial \tilde{Q}}{\partial t} + \frac{\partial \tilde{M}}{\partial z} = \tilde{G}, \qquad (\text{A } 20)$$

$$\frac{\partial \tilde{M}}{\partial t} + \gamma_m \frac{\partial}{\partial z} \left(\frac{\tilde{M}^2}{\tilde{Q}} \right) = \delta_m \frac{\tilde{M}^3}{\tilde{Q}^3} + 2\theta_m \frac{\tilde{M}\tilde{G}}{\tilde{Q}}, \qquad (\text{A } 21)$$

$$\frac{\partial \tilde{G}}{\partial t} + \theta_m \frac{\partial}{\partial z} \left(\frac{\tilde{M}\tilde{G}}{\tilde{Q}} \right) = 0. \qquad (\text{A } 22)$$

In these expressions there are three factors (here assumed constant) given by

$$\gamma_m = \frac{\tilde{Q}}{\tilde{M}^2} \int_0^\infty w^3 \, \mathrm{d}x, \quad \theta_m = \frac{\tilde{Q}}{\tilde{G}\tilde{M}} \int_0^\infty w g' \, \mathrm{d}x \quad \text{and} \quad \delta_m = -\frac{2\tilde{Q}^3}{\tilde{M}^3} \int_0^\infty \mathcal{J}_m \frac{\partial w}{\partial x} \, \mathrm{d}x. \tag{A 23a–c}$$

Under this description of the dynamics, a typical width scale of the line plume is proportional to $\tilde{Q}^2/\tilde{M}$, and one can derive an evolution for this quantity from (A 20) and (A 21). It is not equivalent to the width of the plume unless the dependent fields are given by 'top-hat' profiles. Also, as explained by Craske & van Reeuwijk (2016), the rate at which this flow mixes with the environment is determined by the closure for the work done by the turbulent stresses (and expressed through δ_m (A.23c)). The three governing equations (A 20)–(A 22), which respectively represent the balance of momentum, energy and buoyancy, share many features with those analysed in the main body of this paper. In particular they feature two shape factors, γ_m and θ_m, the magnitudes of which determine whether the governing system of partial differential equations is strictly hyperbolic and the linear stability of the steady state, as shown in appendix C.

A.2. *Shape factors*

The empirical Gaussian distributions of the dependent fields (A 16) and (A 17) allow the shape factors, S and S_f, to be determined straightaway. We find

$$S = \left(\frac{2}{\pi} \right)^{1/2} \frac{\mu \, \mathrm{erf}(\mu\sqrt{2})}{(\mathrm{erf}(\mu))^2}, \qquad (\text{A } 24)$$

$$S_f = \left(\frac{4\gamma^2}{\pi(\gamma^2 + 1)} \right)^{1/2} \frac{\mu \, \mathrm{erf}(\mu(\gamma^2 + 1)^{1/2})}{\mathrm{erf}(\mu)\mathrm{erf}(\mu\gamma)}. \qquad (\text{A } 25)$$
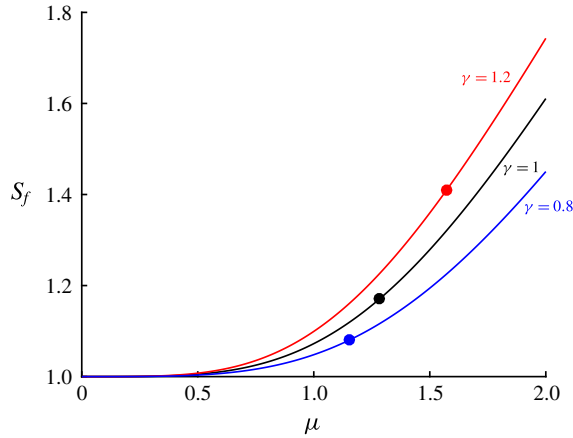
FIGURE 8. (Colour online) The shape factor, S_f, as a function of the scaled width parameter, μ, for various ratios γ (see (A 25)). Also plotted are the parameter values, (μ, S_f), for each value of γ at which the line plume equations first become linearly stable to harmonic disturbances at the source to their steady state.

(Note that $S = S_f$ when $\gamma = 1$.) We plot the shape factor, S_f, as function of μ for various values of the ratio, γ in figure 8. We note that for these Gaussian distributions, both shape factors exceed unity. However, when $\mu = 1$, which corresponds to the choice of the half-width being the e-folding length scale in the distribution (A 16), this leads to $S = 1.0724$. This value of S is not sufficiently large to yield a stable response to harmonic disturbances of the source (see (3.14)). We also plot as a discrete point on each curve in figure 8, the value of μ at which the shape factors S and S_f first lie within the region $R1$ of figure 1, which corresponds to a stable response of the governing equations to a harmonic disturbance at the source of the steady line plume. We note that if the vertical velocity and reduced gravity fields have Gaussian distributions, the half-width must be further from the centreline than the e-folding length scale, and the velocity at the edge less than $1/\mathrm{e}$ of the maximum, for the governing system to be stable.

Appendix B. Linearised perturbation when $S = 1$

In this appendix we derive the solution for the linearised evolution of perturbations to the steady line plume solutions (3.2) when the shape factor $S = 1$. This analysis confirms the asymptotic forms in the far field deduced in § 3 and moreover presents a simple analytical expression for the dependent variables. Denoting the perturbation by $q_1 = (b_1(\xi), q_1(\xi), g_1(\xi))\mathrm{e}^{\mathrm{i}\tau}$, we find from (3.2) that the linearised governing equations are given by

$$\frac{\partial q_1}{\partial \xi} + \left(\frac{1}{\xi} + \mathrm{i}\right) b_1 = 0, \tag{B 1}$$

$$-\frac{\partial b_1}{\partial \xi} + 2\frac{\partial q_1}{\partial \xi} + \frac{1}{\xi}(-b_1 + 2q_1 - g_1) + \mathrm{i}q_1 = 0, \tag{B 2}$$

$$-S_f\frac{\partial b_1}{\partial \xi} + S_f\frac{\partial q_1}{\partial \xi} + S_f\frac{\partial g_1}{\partial \xi} + \mathrm{i}g_1 = 0. \tag{B 3}$$

Then writing $\Phi = q_1 - b_1$ and eliminating between these partial differential equations (B 1)–(B 2), we find that

$$\left(S_f \frac{\partial}{\partial \xi} + \mathrm{i} \right) \left(\xi \frac{\partial}{\partial \xi} + \mathrm{i}\xi + 2 \right) \Phi + S_f \frac{\partial \Phi}{\partial \xi} = 0. \tag{B 4}$$

Provided $S_f \neq 1$, this has a solution that is bounded at the origin,

$$\Phi = c\mathrm{e}^{-\mathrm{i}\xi} \mathcal{M} \left(\frac{3S_f - 2}{S_f - 1}, 4; \frac{\mathrm{i}(S_f - 1)\xi}{S_f} \right), \tag{B 5}$$

where c is a constant, which can be set equal to unity without loss of generality, and $\mathcal{M}(a, b; z)$ is a Kummer function of the first kind (Abramowitz & Stegun 1964). The dependent variables b_1, q_1 and g_1 can be derived from Φ using (B 1)–(B 3); in particular we find that

$$q_1 = \frac{\mathrm{e}^{-\mathrm{i}\xi}}{\xi} \int_0^\xi \Phi(s)(1 + \mathrm{i}s)\mathrm{e}^{\mathrm{i}s} \, \mathrm{d}s, \tag{B 6}$$

$$g_1 = \left(\xi \frac{\partial}{\partial \xi} + \mathrm{i}\xi + 2 \right) \Phi, \tag{B 7}$$

where we have chosen to enforce $q_1(0) = 0$. It is noteworthy that because the governing system is parabolic when $S = 1$ we cannot impose independent values of all the dependent variables at the origin. For example, if $g_1(0) = 1$ then $\Phi(0) = 1/2$ and so not both of b_1 and q_1 can vanish.

The far-field behaviour ($\xi \gg 1$) is determined by the asymptotic behaviour of Φ (and $\mathcal{M}$; see Abramowitz & Stegun (1964)) and thus given by

$$q_1 \sim -\mathrm{i}\mathrm{e}^{-\mathrm{i}\xi} \left(\frac{S_f}{S_f - 1} \right)^{a-1} \frac{\Gamma(4)}{\Gamma(4 - a)} \xi^{1-a}, \tag{B 8}$$

where $a = (3S_f - 2)/(S_f - 1)$. Algebraic growth or decay in the far field is determined by the sign of $1 - a = (2S_f - 1)/(1 - S_f)$, a result that confirms the analysis of § 3 and the result (3.20). Stability thus requires that $S_f < 1/2$.

When $S_f = 1$ the solution takes a different form from (B 5); we find that, up to an arbitrary multiplicative constant,

$$\Phi = \mathrm{e}^{-\mathrm{i}\xi} \frac{\mathrm{J}_3((1 - \mathrm{i})\sqrt{2\xi})}{\xi^{3/2}}, \tag{B 9}$$

where J_3 is a Bessel function of third order (Abramowitz & Stegun 1964). In the far field ($\xi \gg 1$) we find that

$$q_1 \sim \frac{\mathrm{i}\mathrm{e}^{\mathrm{i}\pi/8}}{2\sqrt{\pi}} \frac{\mathrm{e}^{-\mathrm{i}\xi + (1+\mathrm{i})\sqrt{2\xi}}}{\xi^{5/4}}. \tag{B 10}$$

This confirms the analysis of § 3 and the result (3.29), which shows that the system is ill-posed when both the shape factors are equal to unity.

Appendix C. Linear stability of alternative models of line plumes

In this appendix, we apply the methodology of §3 to investigate the linear stability of pure plume solutions of the governing equations developed for line jets by Craske (2017), extended to linear plumes and given by (A 20)–(A 22) on the assumption that the shape factors θ_m and γ_m and the energy closure coefficient, δ_m are constants. It is convenient to substitute for the dependent variables as follows:

$$\tilde{Q} = \theta_m \Lambda^2 f_1^{1/3} z \tilde{q}(\xi, \tau), \quad \tilde{M} = \Lambda f_1^{2/3} z \tilde{m}(\xi, \tau) \quad \text{and} \quad \tilde{G} = \Lambda f_1^{2/3} \tilde{g}(\xi, \tau), \quad (C\,1a\text{--}c)$$

where $2f_1$ is the dimensional buoyancy flux per unit width delivered by the source and $\Lambda^3 = \delta_m/(\theta_m^2(\gamma_m - 2\theta_m))$. The dimensionless independent variables are $\tau = t/T$ and $\xi = z/(\Lambda f^{1/3} T)$, where T is a dimensional time scale of the motion (which in the calculation that follows is set by the angular frequency of the harmonic disturbance to the source). The expressions are the equivalent of (2.13); the factors multiplying $\tilde{q} = (\tilde{q}, \tilde{m}, \tilde{g})$ are the steady state that results from the sustained imposition of the steady flux at the source. The expressions feature the two shape factors in the governing equation (A 20)–(A 22), namely γ_m and θ_m and the parameter, δ_m, that emerges from the simple closure of the magnitude of the turbulent terms. The governing equations can then be written in compact form

$$\frac{\partial \tilde{q}}{\partial \tau} + \begin{pmatrix} 0 & 1 & 0 \\ -\gamma_m \tilde{m}^2/\tilde{q}^2 & 2\gamma_m \tilde{m}/\tilde{q} & 0 \\ -\theta_m \tilde{m}\tilde{g}/\tilde{q}^2 & \theta_m \tilde{g}/\tilde{q} & \theta_m \tilde{m}/\tilde{q} \end{pmatrix} \frac{\partial \tilde{q}}{\partial \xi}$$
$$= \frac{1}{\xi} \begin{pmatrix} \tilde{g} - \tilde{m} \\ (\gamma_m - 2\theta_m)\tilde{m}^3/\tilde{q}^3 + 2\theta_m \tilde{m}\tilde{g}/\tilde{q} - \gamma_m \tilde{m}^2/\tilde{q} \\ 0 \end{pmatrix}. \quad (C\,2)$$

The steady state corresponds to $\tilde{q} = (1, 1, 1)$.

We explore the linear stability of the steady state to harmonic perturbation at the source. As in §3, we non-dimensionalise times with respect to the angular frequency of the perturbation and write $\tilde{q} = (1, 1, 1) + \epsilon \tilde{q}_1$, where ϵ is a small ordering parameter. Then following §3, we study the linearised response in the far field, by substituting $\tilde{q} = \exp(\phi(\xi) + i\tau)\psi(\xi)$. Then the governing equation (C 2) is given by

$$\boldsymbol{A}\frac{d\psi}{d\xi} + \left(\boldsymbol{A}\frac{\partial\phi}{\partial\psi} + \boldsymbol{C}\frac{1}{\xi} + i\boldsymbol{I}\right)\psi = 0, \quad (C\,3)$$

where the matrices $\boldsymbol{A}$ and $\boldsymbol{C}$ are given by

$$\boldsymbol{A} = \begin{pmatrix} 0 & 1 & 0 \\ -\gamma_m & 2\gamma_m & 0 \\ -\theta_m & \theta_m & \theta_m \end{pmatrix} \quad \text{and} \quad \boldsymbol{C} = \begin{pmatrix} 0 & -1 & 1 \\ 4\theta_m - 2\gamma_m & \gamma_m - 4\theta_m & 2\theta_m \\ 0 & 0 & 0 \end{pmatrix}. \quad (C\,4a,b)$$

The amplitude of the disturbance grows or decays algebraically in the far field ($\xi \gg 1$) with exponent σ_i ($i = 1, 2, 3$). The determination of these exponents follows the method set out in §3 and relies upon the eigenvectors of $\boldsymbol{A}$ (which are identical to (3.7) and (3.9) on replacing S and S_f with γ_m and θ_m, respectively). This leads to the following results:

$$\sigma_1 = \frac{2\theta_m^2 - 3\theta_m + \gamma_m}{\theta_m^2 - 2\theta_m\gamma_m + \gamma_m}, \quad (C\,5)$$

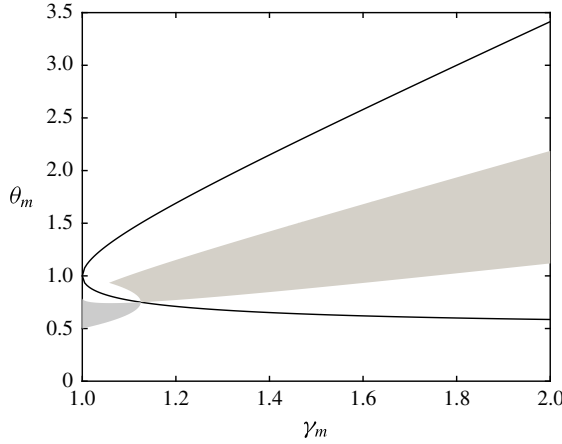FIGURE 9. The regions of the plane of shape factors, (γ_m, θ_m), for which the steady line plume solution (C 1) is linearly stable to harmonic disturbances to the source (shaded region, corresponding to $\sigma_i < 0$, $i = 1$–3). Also plotted are the parameter values for which the governing system of equations is ill-posed (solid lines).

$$\sigma_{2,3} = \frac{\pm(3\theta_m - \gamma_m)(\gamma_m^2 - \gamma_m)^{1/2} - 6\theta_m^2 + 6\theta_m\gamma_m - \gamma_m^2}{2\gamma_m(\theta_m - \gamma_m \mp (\gamma_m^2 - \gamma_m)^{1/2})}. \tag{C 6}$$

Thus there are regions in the (γ_m, θ_m)-plane for which the pure plume solution is linearly stable and these are depicted in figure 9. Furthermore the system is ill-posed when $\theta_m = \gamma_m \pm (\gamma_m^2 - \gamma_m)^{1/2}$ and this includes the special case of $\theta_m = \gamma_m = 1$ that corresponds to an assumption of 'top-hat' profiles for the dependent variables.

Overall the results for this alternative system of governing equations share qualitative similarities with those analysed in the main body of the text, although there are quantitative differences. The systems both feature two shape factors and are ill-posed if top-hat profiles are assumed. Linear stability occurs for regions within the plane of shape factors determined by this analysis (see figures 1 and 9).

Appendix D. Instantaneous changes in buoyancy flux per unit width at the source ($S_f < S - \sqrt{S^2 - S}$)

When the shape factors are drawn from the region $R2$ (see figure 1) in which $S_f < S - \sqrt{S^2 - S}$ and the governing equation is both well-posed and stable, additional phenomenology can occur during the unsteady adjustment of the plume arising from an instantaneous change in buoyancy flux at the origin. To illustrate these effects we select $(S, S_f) = (1.1, 0.5)$ and we examine both an increase $\mathcal{F} = 0.1$ and a decrease $\mathcal{F} = 5$ in the buoyancy flux at the source.

First we compute the solutions by direct numerical integration of the governing system of (3.2) and the results are plotted in figures 10. As for the previous examples (§ 4), the nonlinear adjustment from one state to another proceeds via an unsteady pulse that advects through the domain. We note that an increase in buoyancy flux leads to a broadening of the plume as the flow decelerates to match the far field, pre-existent conditions and conversely the plume narrows for a decrease in buoyancy flux as the plume accelerates to match the far field. In addition, however, when the source flux increases ($\mathcal{F} < 1$) there are now two shocks in the profiles of the dependent variables
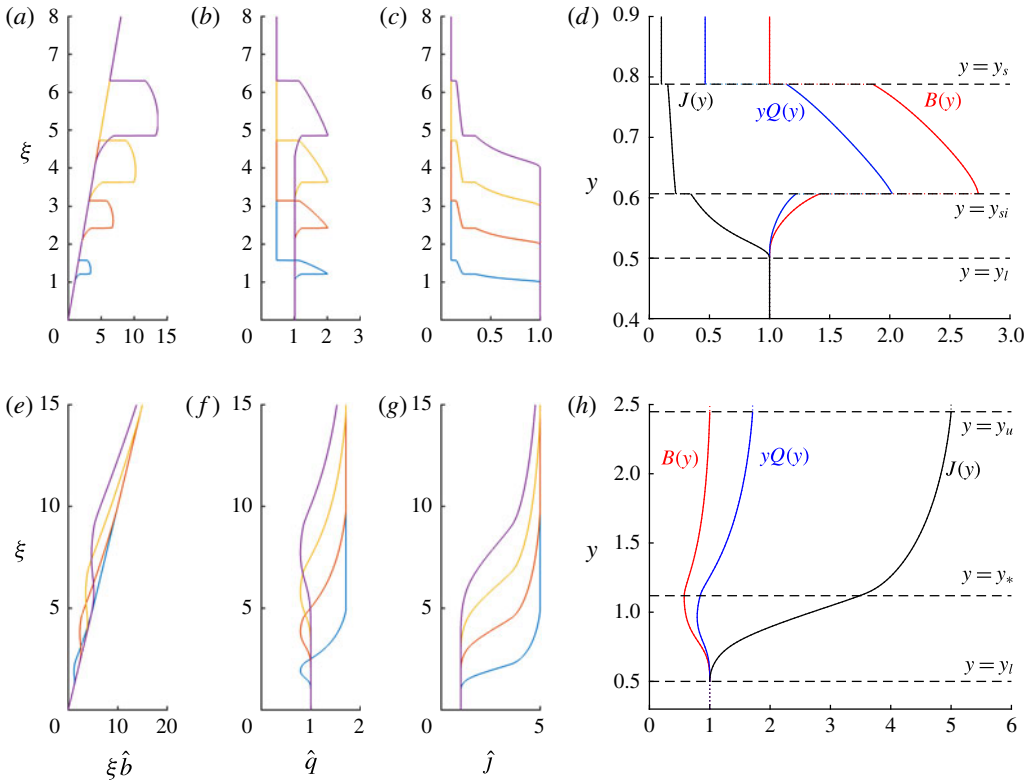
FIGURE 10. (Colour online) (*a–c*), (*e–g*) The rescaled width $\xi\hat{b}(\xi)$, volume flux $\hat{q}(\xi)$ and buoyancy flux $\hat{j}(\xi)$ as functions of the dimensionless distance from source, ξ, at dimensionless times $\tau = 2, 4, 6$ and 8 for (*a–c*) an instantaneous increase in the buoyancy flux per unit width at the origin ($\mathcal{F} = 0.1$), and (*e–g*) an instantaneous decrease in the buoyancy flux per unit width at the origin ($\mathcal{F} = 5$). (*d,h*) The similarity solutions for $B(y)$, $Q(y)$ and $J(y)$ as functions of the similarity variable, y (solid lines) and the results from the direct numerical integration of the governing equations (3.2) (dotted lines) for (*d*) $\mathcal{F} = 0.1$ and (*h*) $\mathcal{F} = 5$. Note that the similarity solution and the direct numerical integration are virtually indistinguishable. Also shown are important locations in the construction of the similarity solution: (*d*) (y_l, y_{si}, y_s) and (*h*) (y_l, y_*, y_u). In these computations, $S = 1.1$ and $S_f = 0.5$.

for an increase in buoyancy flux (e.g. $\mathcal{F} = 0.1$, figure 10(*a–c*), one of which is at the leading edge of the transition zone and the other of which is at an interior location. Also, for a decrease in buoyancy flux (e.g. $\mathcal{F} = 5$, figure 10*e–g*), there is only a continuous solution whereas those flows in §4.3 generate an internal shock.

We may construct the similarity solutions for a flow with an increased source strength $\mathcal{F} < 1$ as follows. These solutions first diverge from the conditions associated with the new source at $y = y_l = S_f$ at which location $B = 1$, $Q = 1/S_f$ and $G = 1/S_f^2$ (see (4.3)). There is an internal shock at $y = y_{si}$ and a shock at the leading edge at $y = y_s$, beyond which the dependent variables adopt their far-field forms (4.2); both y_{si} and y_s are unknown and must be determined as part of the solution. We form the solution by guessing values for y_{si} and y_s and then integrating from $y = y_s$ to $y = y_l$, using the shock conditions (4.4) to evaluate the change in the variables across the two discontinuities. We then iteratively adjust the unknown values until

$B(y_l) - 1$ and $Q(y_l) - 1/S_f$ vanish. The similarity solution for $\mathcal{F} = 0.1$ is plotted in figure 10(*d*), together with results from the numerical integration of the governing partial differential equations, which we note are virtually indistinguishable.

When the buoyancy flux at the origin is instantaneously decreased, $\mathcal{F} > 1$, the similarity solution varies continuously between $y = y_l = S_f$ and $y = y_u = \mathcal{F}^{1/3}(S + \sqrt{S^2 - S})$. For $y < y_l$, the solution is given by (4.3), while for $y > y_u$, it is given by (4.2). Between y_l and y_u, there is a location $y = y_*$ at which (4.1) is singular and $W = 1/\mu_-$. The solution close to $y = y_l$ is given by the power series (4.13), while the solution close to y_u is given by (4.5), and these allow the dependent variables to be integrated away from the singular points. Both series expansions feature an undetermined constant multiplying a term featuring the non-integer power. The solution is then constructed by iteratively adjusting these constants until a continuous solution is found such that $W = 1/\mu_-$ at $y = y_*$. The solution is plotted in figure 10(*h*) and we again observe that the similarity solution and numerical integration are indistinguishable.

REFERENCES

ABRAMOWITZ, M. & STEGUN, I. 1964 *A Handbook of Mathematical Functions*, Applied Mathematics Series, vol. 55. National Bureau of Standards.

ANWAR, H. O. 1969 Experiment on an effluent discharging from a slot into stationary or slow moving fluid of greater density. *J. Hydraul. Res.* **7**, 411–431.

BAKER, E. T., MASSOTH, G. J., FEELY, R. A., EMBLEY, R. W., THOMSON, R. E. & BURD, B. J. 1995 Hydrothermal event plumes from the CoAxial seafloor eruption site, Juan de Fuca Ridge. *Geophys. Res. Lett.* **22**, 147–150.

BRADBURY, L. J. S. 1965 The structure of a self-preserving turbulent plane jet. *J. Fluid Mech.* **23**, 31–64.

VAN DEN BREMER, T. S. & HUNT, G. R. 2014 Two-dimensional planar plumes and fountains. *J. Fluid Mech.* **750**, 210–244.

CHING, C. Y., FERNANDO, H. J. S. & ROBLES, A. 1995 Breakdown of line plumes in turbulent environments. *J. Geophys. Res.* **100**, 4707–4713.

CRASKE, J. 2017 The properties of integral models for planar and axisymmetric unsteady jets. *IMA J. Appl. Maths* **82**, 305–333.

CRASKE, J. & VAN REEUWIJK, M. 2016 Generalised unsteady plume theory. *J. Fluid Mech.* **792**, 1013–1052.

GLAZE, L. S., BALOGA, S. M. & WIMERT, J. 2011 Explosive volcanic eruptions from linear vents on Earth, Venus, and Mars: comparisons with circular vent eruptions. *J. Geophys. Res.* **116**, E01011.

KAMINSKI, E. L., TAIT, S. & CARAZZO, G. 2005 Turbulent entrainment in jets with arbitrary buoyancy. *J. Fluid Mech.* **526**, 361–376.

KURGANOV, A., NOELLE, S. & PETROVA, G. 2001 Semi-discrete central-upwind schemes for hyperbolic conservation laws and Hamilton–Jacobi equations. *SIAM J. Sci. Comput.* **23**, 707–740.

LEE, S. & EMMONS, H. W. 1961 A study of natural convection above a line fire. *J. Fluid Mech.* **11**, 353–368.

LINDEN, P. F. 2000 Convection in the environment. In *Perspectives in Fluid Dynamics* (ed. H. K. Moffatt, G. K. Batchelor & M. G. Worster), pp. 289–345. Cambridge University Press.

MORTON, B. R., TAYLOR, G. I. & TURNER, J. S. 1956 Turbulent gravitational convection from maintained and instantaneous source. *Proc. R. Soc. Lond.* A **234**, 1–23.

PRIESTLEY, C. H. B. & BALL, F. K. 1955 Continuous convection from an isolated source of heat. *Q. J. R. Meteorol. Soc.* **81**, 144–157.

ROUSE, H., YIH, C. S. & HUMPHREYS, H. W. 1952 Gravitational convection from a boundary source. *Tellus* **4**, 201–210.

SCASE, M. M., CAULFIELD, C. P., DALZIEL, S. B. & HUNT, J. C. R. 2006 Time-dependent plumes and jets with decreasing source strengths. *J. Fluid Mech.* **563**, 443–461.

SCASE, M. M. & HEWITT, R. E. 2012 Unsteady turbulent plume models. *J. Fluid Mech.* **697**, 455–480.

STOTHERS, R. B. 1989 Turbulent atmospheric plumes above line sources with an application to volcanic fissure eruptions on the terrestrial planets. *J. Atmos. Sci.* **46**, 2662–2670.

TURNER, J. S. 1973 *Buoyancy Effects in Fluids*. Cambridge University Press.

TURNER, J. S. 1986 Turbulent entrainment: the development of the entrainment assumption and its application to geophysical flows. *J. Fluid Mech.* **173**, 431–471.

WHITHAM, G. B. 1974 *Linear and Nonlinear Waves*. Wiley.

WOODHOUSE, M. J., PHILLIPS, J. C. & HOGG, A. J. 2016 Unsteady turbulent buoyant plumes. *J. Fluid Mech.* **794**, 595–639.

WOODS, A. W. 2010 Turbulent plumes in nature. *Annu. Rev. Fluid Mech.* **42**, 391–412.